# Low-temperature crystallography and vibrational properties of rozenite (FeSO<sub>4</sub>·4H<sub>2</sub>O), a candidate mineral component of the polyhydrated sulfate deposits on Mars

JOHANNES M. MEUSBURGER<sup>1,2,3,†</sup>, KAREN A. HUDSON-EDWARDS<sup>1,‡</sup>, CHIU C. TANG<sup>2</sup>, EAMONN T. CONNOLLY<sup>2</sup>, RICH A. CRANE<sup>1</sup>, AND A. DOMINIC FORTES<sup>3,\*</sup>

<sup>1</sup>Camborne School of Mines and Environment and Sustainability Institute, Tremough Campus, University of Exeter, Penryn TR10 9EZ, U.K.

<sup>2</sup>Diamond Light Source, Harwell Science and Innovation Campus, Fermi Avenue, Didcot OX11 0DE, U.K.

<sup>3</sup>ISIS Neutron and Muon Source, STFC Rutherford Appleton Laboratory, Harwell Science and Innovation Campus, Chilton, Didcot,
Oxfordshire OX11 0QX, U.K.

#### ABSTRACT

Rozenite (FeSO<sub>4</sub> 4H<sub>2</sub>O) is a candidate mineral component of the polyhydrated sulfate deposits on the surface and in the subsurface of Mars. To better understand its behavior at temperature conditions prevailing on the Martian surface and aid its identification in ongoing and future Rover missions, we have carried out a combined experimental and computational study of the mineral's structure and properties. We collected neutron powder diffraction data at temperatures ranging from 21-290 K, room-temperature synchrotron X-ray data and Raman spectra. Moreover, first-principles calculations of the vibrational properties of rozenite were carried out to aid the interpretation of the Raman spectra. We found, in contrast to a recent Raman spectroscopic study, that there are no phase transitions between 21 and 290 K. We confirm the heavy atom structure reported in the literature (space group  $P2_1/n$ ) to be correct and present, for the first time, an unconstrained determination of the H atom positions by means of high-resolution neutron powder diffraction, and report the complete crystal structure at 290 and 21 K. The anisotropy of the thermal expansion of the lattice vectors is  $\alpha_a$ :  $\alpha_b$ :  $\alpha_c = 1.00:2.19:1.60$  at 285 K. Subsequent analysis of the thermal expansion tensor revealed highly anisotropic behavior as reflected in negative thermal expansion approximately  $\|\langle 101 \rangle$  and ratios of the tensor eigenvalues of  $\alpha_1:\alpha_2:\alpha_3=-1:3.74:5.40$  at 285 K. Lastly, we demonstrated how combining Raman spectroscopy and X-ray diffraction of the same sample sealed inside a capillary with complementary first-principles calculations yields accurate reference Raman spectra. This workflow enables the construction of a reliable Raman spectroscopic database for planetary exploration, which will be invaluable to shed light on the geological past as well as in identifying resources for the future colonization of planetary bodies throughout the solar system.

**Keywords:** Polyhydrated sulfates, Mars, rozenite, negative thermal expansion, Raman spectroscopy, density functional theory, neutron diffraction, synchrotron X-ray diffraction

#### Introduction

Ferrous sulfate minerals occur in various hydration states, FeSO<sub>4</sub>·nH<sub>2</sub>O with n = 1, 4, 5, 6, 7, most commonly in the vicinity of sulfide ore deposits (Jambor et al. 2000). In such environments, weathering of ore and waste materials releases oxidized iron and sulfur, as well as a wide range of potentially toxic elements, into nearby surface waters (Hudson-Edwards et al. 1999; Nordstrom 2011), which subsequently precipitate as hydrous ferric and ferrous sulfates. Widespread occurrences of minerals diagnostic to acid mine drainage environments have been identified on the Martian surface using both surface (Klingelhöfer et al. 2004) and orbit (Carter et al. 2013) based measurements. These findings have been interpreted as evidence for the existence of acidic aquatic environments early in Martian history (Squyres et al. 2004). In detail, it has been proposed that hydrated sulfate minerals on Mars are secondary minerals produced by the evaporation of fluids involved in the aqueous alteration of Martian basalt (Tosca et al. 2005). In the Valles Marineris canyon system sulfate minerals occur in sandy stratified deposits, typically exposed in canyon walls, and lie stratigraphically above widespread clay-mineral deposits (Roach et al. 2010). This stratigraphic sequence records a transition from neutral-alkaline (clay-forming) to acidic (iron sulfate-forming) aqueous environments indicating a change in global climate from wetter to dryer conditions starting around 4 Gya (Bibring et al. 2006). Due to their apparent role as climatological archives, a detailed mineralogical characterization of these sulfate deposits is essential to decipher the nature and drivers of changing environmental conditions during the planet's early history. However, attempts to assign any single mineral species to the spectral data acquired for the polyhydrated sulfate deposits have proven to be challenging. This is due to inherent difficulty in differentiating between the diffuse near-IR reflectance spectra of different sulfate phases in the range 0.35–5.1 µm [corresponding to the OMEGA] spectrometer on-board the Mars Express orbiter (Langevin et al. 2006)] that is typically measured from orbit, i.e., significant spectral similarities occur between sulfates of different chemical composition and degrees of hydration (Bishop et al. 2009).

Numerous studies have been carried out to identify candidate minerals for the polyhydrated sulfate phase. If these deposits indeed originate from the alteration of olivine in Martian basalt, the

<sup>\*</sup> E-mail: dominic.fortes@stfc.ac.uk

<sup>†</sup> Orcid 0000-0003-4367-3566

<sup>‡</sup> Orcid 0000-0003-3965-2658

polyhydrated sulfate phase as its weathering product would likely be an iron- or magnesium-bearing sulfate (Bibring et al. 2005) or a sulfate mineral of intermediate composition. Among the iron sulfates, Carter et al. (2013) noted that rozenite matched the data acquired by OMEGA and CRISM very well. Wang et al. (2016), however, observed by studying the phase stability of melanterite (FeSO<sub>4</sub>·7H<sub>2</sub>O), under variable temperature and relative humidity conditions, that at 323 K rozenite merely occurs as a transient state and further dehydrates to szomolnokite (FeSO<sub>4</sub>·H<sub>2</sub>O). Based on this finding, they concluded that rozenite is not stable under present day Martian surface conditions. Nevertheless, we note that in the same study Wang et al. (2016) reported that even after around 2030 h [number obtained from supporting information S4 in Wang et al. (2016)] of exposure to relatively dry air (i.e., 33% relative humidity) rozenite did not reveal any signs of dehydration at temperatures as high as 294 K, which is well above a maximum ground temperature of 280 K measured by the Curiosity rover over the first 100 sols of data acquisition (Gómez-Elvira et al. 2014). Moreover, rehydration of szomolnokite to rozenite and melanterite was observed at 298 K at a relative humidity of 65% (Mitchell 1984). Hence, even if temperatures as high as 323 K have prevailed at any point in Martian history (leading to the dehydration of rozenite or melanterite), the process may have been reversed under present day Martian environmental conditions. Thus, rozenite should still be regarded as a promising candidate mineral for the polyhydrated sulfate phase.

To unambiguously confirm the absence or presence of rozenite in the Martian polyhydrated sulfate deposits, in situ analytical techniques such as X-ray diffraction and Raman spectroscopy are needed. Raman spectroscopy in particular has proven very effective in discriminating between various sulfate mineral species (Košek et al. 2017), and thus appears well suited to unravel the mineralogical phase composition of the polyhydrated sulfate phase. Raman spectroscopic investigations of the Martian soil have recently become possible. NASA's Perseverance Rover, landing on the Martian surface in spring 2021, as well as the ESA's Rosalind Franklin Rover, which will likely arrive on Mars in 2023, both feature Raman spectrometers [Rosalind Franklin: The Raman Laser Spectrometer (Rull et al. 2017); Perseverance: SuperCam (Wiens et al. 2021); and SHERLOC (Bhartia et al. 2021)] as part of their scientific payload.

Interestingly, Chio et al. (2007) observed an apparent splitting of Raman-active vibrational modes of rozenite, which they suggested might be indicative of two structural phase transitions ( $T_{\rm crit1} = 240$ –190 K,  $T_{\rm crit2} = 140$ –90 K). The first transition is well within the range of temperatures relevant to the Martian surface. Although Raman spectroscopy is a powerful tool for the identification of polymorphic phase transitions, sharpening of closely spaced vibrational modes at low temperatures might be erroneously interpreted as splitting due to a phase transition.

With rozenite being one of the most promising candidates for the polyhydrated sulfate phase on the Martian surface, there is an interest in revisiting these putative phase transitions by means of neutron diffraction to determine the structural stability of rozenite at temperatures relevant to the Martian surface as well as to solve the crystal structure of any proposed low-temperature polymorphs. For this reason, we have studied herein the structural stability of  $FeSO_4\cdot 4D_2O$  at temperatures ranging from 290 K down to 21 K by

means of high-resolution time-of-flight (TOF) neutron diffraction. Furthermore, the samples used for the neutron diffraction have been perdeuterated for the explicit reason of avoiding the large incoherent scattering signal from ordinary <sup>1</sup>H, which produces a substantial background masking weak Bragg peaks. Use of <sup>2</sup>D virtually eliminates this background and allows for rapid acquisition of high-quality data.

Since subtle changes in relative humidity may cause hydrated sulfates to partially or completely re- or dehydrate (Wang et al. 2016), it is entirely possible that the rozenite sample studied by Chio et al. (2007) underwent a transformation in between the initial phase identification by X-ray diffraction and the subsequent measurements of its vibrational properties. To confirm that the Raman spectra reported by Chio et al. (2007) indeed correspond to rozenite, we have carried out Raman spectroscopy and synchrotron X-ray diffraction, which are able to detect the smallest amounts [i.e., 0.1 wt% (Thompson et al. 2009)] of any contaminant phases. Such measurements have been complemented with ab initio calculations to further explore the vibrational properties of rozenite. This combined experimental and theoretical approach allows us to cast light on the structural stability of rozenite at Martian surface temperatures and, therefore, will aid the identification of rozenite in future and ongoing Mars missions.

#### **METHODS**

#### Synthesis and phase analysis

FeSO<sub>4</sub>·7H<sub>2</sub>O (Sigma Aldrich ACS reagent grade) was dehydrated under vacuum for 48 h at 473 K to prepare anhydrous FeSO<sub>4</sub>. A hot supersaturated solution of FeSO<sub>4</sub> in 0.5 M D<sub>2</sub>SO<sub>4</sub> (Sigma Aldrich >99 atom% D) was then cooled to room temperature to precipitate fine-grained FeSO<sub>4</sub>·7D<sub>2</sub>O. The sealed container was stored for several years, during which time diurnal and seasonal temperature changes resulted in the finegrained material altering into a fully dense coarse crystalline material. FeSO4:7D2O crystals were then ground to a powder under helium to prevent exchange of 2D with atmospheric 1H. The powder was loaded into rubber-sealed glass jars containing a saturated solution of MgCl2 in D2O (Sigma Aldrich >99 atom% D), which buffered the relative humidity at 33% (Greenspan 1977), and kept at 280 K for 3 days. The sample was then transferred, again under helium, into the sample holder used for the neutron diffraction experiments. This comprised an aluminum frame surrounding a cuboid sample cavity of dimensions  $18 \times 23 \times 10$  mm (w × h × d), open at the front and back. The rear opening was first covered with a vanadium foil window sealed by indium wire; powder was then transferred into the sample holder and the front opening was sealed with another vanadium foil window. Gadolinium and cadmium foils were used to mask scattering from various aluminum and steel parts that might be exposed to the incident neutron beam around the edges of the vanadium windows. A cartridge heater, used for temperature control, and a RhFe thermometer were inserted into the aluminum frame of the sample container either side of the sample.

The sample was mounted into a closed cycle refrigerator (CCR) at the High-Resolution Powder Diffraction (HRPD) beamline, ISIS Neutron and Muon Spallation Facility, U.K. This instrument allows collection of neutron time-of-flight (TOF) data in various 100 ms wide "windows"; those used in this study were 30–130 and 100–200 ms. In HRPD's highest resolution backscattering detectors ( $2\theta = 154-176^\circ$ ), these yield diffraction patterns covering d-spacings from 0.65–2.60 and 2.20–3.90 Å, respectively. The latter is often best used for rapid phase identification, even though the incident neutron flux is very low, since Bragg peaks are typically fewer and better dispersed while also being rather more intense than those at shorter d-spacings.

We could thus quickly confirm that the sample was mostly rozenite, but with a few weak Bragg peaks identified as melanterite, indicating that dehydration of the starting material was incomplete. Heating the sample to 305 K for 60 min and then 315 K for a further 20 min resulted in the complete transformation of melanterite to rozenite. At 315 K, however, the high temperatures also gave rise to slight further dehydration and the formation of szomolnokite. Therefore, we lowered the temperature again to 305 K and kept the sample at this temperature for a further 12 min to ensure the complete transformation from melanterite to rozenite in the final sample material. The diffraction patterns acquired during dehydration of the sample are provided in the Online Materials Figure S1. Rietveld refinement of the neutron

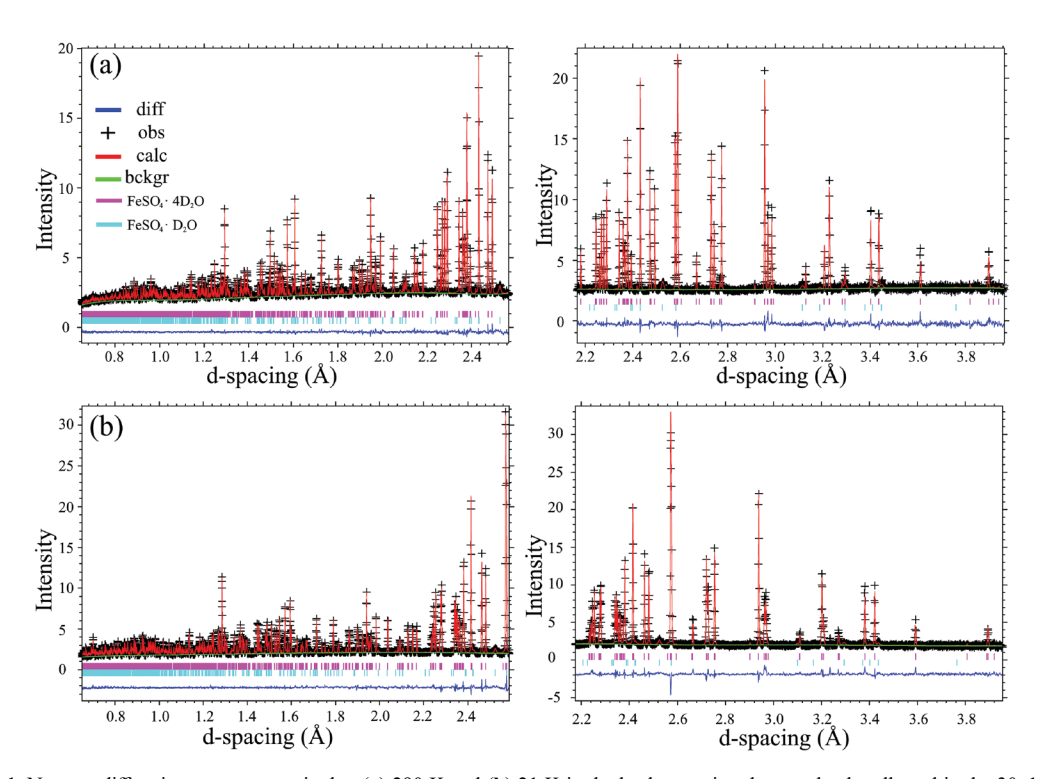


FIGURE 1. Neutron diffraction patterns acquired at (a) 290 K and (b) 21 K in the backscattering detector bank collected in the 30–130 (left) and 100–200 ms (right) TOF window. The observed data plotted as crosses, the red line represents the fitted model, and the blue line the difference profile. The tick marks corresponding to each of the Bragg peaks of FeSO<sub>4</sub>·4D<sub>2</sub>O and FeSO<sub>4</sub>·D<sub>2</sub>O are displayed in magenta and cyan, respectively. (Color online.)

diffraction pattern acquired at 290 K suggests that the final sample material consists of 93.5(1) wt% rozenite and 6.5(1) wt% szomolnokite.

Protiated FeSO<sub>4</sub>·4H<sub>2</sub>O for the synchrotron X-ray diffraction and Raman analysis was synthesized using the dehydration method stated above. We placed the reagent FeSO<sub>4</sub>·7H<sub>2</sub>O in a rubber-sealed glass jar containing a saturated solution of MgCl<sub>2</sub> in H<sub>2</sub>O for 3 days at around 290 K. Subsequently, the sample was loaded into a borosilicate glass capillary of 0.5 mm diameter. The loaded specimen and the rest of the sample material were used for Raman analysis.

### **TOF neutron diffraction and Rietveld refinement**

High-resolution TOF neutron diffraction data were collected at temperatures ranging from 315 to 21 K upon cooling and warming. After the initial dehydration at 305 and 315 K, the sample was cooled to 290 K. Data sets with long counting times of 3 h 17 min in the 30–130 and 100–200 ms TOF window were then collected to allow crystal structure refinement. To characterize the thermal expansion of rozenite, diffraction patterns with shorter counting times of 50 min were collected on cooling in 10 K increments in the 100–200 ms TOF window in the temperature range from 290–21 K. At the base temperature of 21 K, another data set for structural refinement was acquired in the 100–200 ms TOF window, again, for 3 h 17 min and in 30–130 ms window for 4 h 6 min. Lastly, we collected diffraction patterns upon heating from 35–285 K in 10 K increments for 37 min each. To ensure good thermal equilibrium between the heated aluminum frame of the sample holder and the powder sample itself, temperature changes were done at 3 K min<sup>-1</sup> and a dwell time of 10 min after reaching a set-point was used prior to the start of data collection.

The data were time-focused, normalized to the incident spectrum and corrected for instrument efficiency using a V:Nb standard. Diffractometer calibration constants and instrumental peak-profile coefficients were determined using NIST silicon SRM640e and CeO<sub>2</sub> standards.

All refinements were carried out using the Rietveld method (Albinati and Willis 1982; van Laar and Schenk 2018) as implemented in the GSAS/EXPGUI software suite (Toby 2001). The diffraction patterns collected in HRPD's backscattering detector bank at 290 and 21 K are displayed in Figure 1 and the refinement parameters are given in Table 1 as well as in the CIF¹. Clearly, the refined structural models are in excellent agreement with the observed intensity data.

Unit-cell parameters were refined from the shorter 100-200 ms TOF data sets using initial least-squares cycles of Rietveld refinement, followed by a series of

least-squares cycles using the "F(calc) weighted" method; this workflow typically results in the most precise lattice parameters by virtue of fitting the intensities more accurately. For szomolnokite we used the structure reported by Talla and Wildner (2019) for the refinements and varied the lattice parameters and profile coefficients at each temperature. The small number of weak peaks accessible in the 100–200 ms TOF window combined with the low symmetry of szomolnokite precludes us from following the evolution of the lattice parameters accurately as a function of temperature, which are therefore not reported in this study.

#### Synchrotron X-ray diffraction and Raman spectroscopy

A synchrotron X-ray powder diffraction pattern of the protiated rozenite capillary sample was collected at the 111 instrument, Diamond Light Source, U.K. using the Multi Analyzing Crystal detectors (Thompson et al. 2009). The experiment was carried out at an ambient temperature of  $295 \pm 0.5$  K. The wavelength of 0.826574(9) Å and a zero-point error of  $0.000315(2)^\circ$  were determined from a NIST SRM 640c silicon standard.

Raman spectra of protiated rozenite were acquired using a B&W Tek i-Raman Plus spectrometer equipped with a neodymium doped yttrium-aluminum-garnet laser that was frequency-doubled to 532 nm (maximum power of 30 mW as determined by the manufacturer). We collected data over the entire spectral range accessible to the spectrometer (i.e., 65–4200 cm<sup>-1</sup>) with a resolution of smaller than 3.5 cm<sup>-1</sup> (as determined by the manufacturer at 614 nm) on protiated rozenite powder samples both outside and inside of the very same borosilicate glass capillary that was used for the synchrotron diffraction analysis. The spectra were collected for 53 and 50 s and averaged over three acquisitions for the sample outside and inside of the capillary, respectively.

# Ab initio vibrational properties from density functional theory (DFT)

We performed Kohn-Sham DFT calculations (Hohenberg and Kohn 1964; Kohn and Sham 1965) using ultrasoft pseudopotentials from the GBRV library (Garrity et al. 2014). Kinetic energy cut-off values and k-point grid density were derived from convergence testing; values of 70 and 840 Ry were adopted for the wave function and charge density cut-offs, respectively and a Monkhorst-Pack (Monkhorst and Pack 1976) k-point grid of  $2 \times 1 \times 2$  was applied to sample the Brillouin zone.

**TABLE 1.** Selected details of the crystal structure refinement, for a full description we refer to the CIF<sup>1</sup>

Crystal data							
Chemical formula	FeSO <sub>4</sub> ·4D <sub>2</sub> O	FeSO₄·4D₂O					
Space group	P2₁/n	P2₁/n					
Temperature	290 K	21 K					
a (Å)	5.966031(12)	5.942863(15)					
b (Å)	13.609756(31)	13.521390(40)					
c (Å)	7.962529(14)	7.933688(20)					
β (°)	90.4288(2)	89.8617(2)					
V (ų)	646.509(2)	637.516(2)					
Ζ	4	4					
Refinement							
R-factors	Rp = 0.0237, Rwp = 0.0179	Rp = 0.0316, $Rwp = 0.0257$					
Goodness of fit	$\chi^2 = 2.190$	$\chi^2 = 5.472$					
Number of refined parameters	192	182ª					

<sup>&</sup>lt;sup>a</sup> Number of refined parameters is lower for the measurement at 21 K since the background coefficients had to be fixed for the 30–130 ms TOF window.

The crystal structure as reported by Baur (1962) served as input geometry for an initial relaxation using the PBE functional (Perdew et al. 1996) in conjunction with the D2 dispersion correction (Grimme 2006). We have demonstrated in our previous work (Meusburger et al. 2021) that the PBE+D2 approach is very well suited to model geometries at temperatures close to the ground state both for dispersion-dominated solids as well as hydrogen-bonded solids such as the one under investigation.

The unit-cell and internal atomic coordinates were relaxed using the Broyden-Fletcher-Goldfarb-Shanno algorithm (Pfrommer et al. 1997), with convergence thresholds  $1\times 10^{-6}$  Ry,  $1\times 10^{-5}$  Ry/Bohr,  $5\times 10^{-1}$  kbar for the total energy, forces, and pressure, respectively. Moreover, we applied a mixing factor of 0.3 and the local Thomas-Fermi charge mixing mode (Raczkowski et al. 2001) to achieve convergence in the self-consistent field cycles.

The structure optimized at the DFT+D level served as basis for the self-consistent computation of the Hubbard U by means of density functional perturbation theory (Timrov et al. 2018). The formulation of the Hubbard model following Dudarev et al. (1998) as well as nonorthogonalized atomic orbitals (Cococcioni and de Gironcoli 2005; Amadon et al. 2008) as projectors for the strongly localized 3d states of Fe<sup>2+</sup> were used for all DFT+U calculations. We have tested multiple q-meshes and found that a grid of  $2\times1\times2$  is necessary to derive Hubbard U values converged to within 0.0007 eV. Subsequently, we used the U value converged with respect to the q-mesh (i.e., 6.9806 eV), and again, computed the U value from this optimized structure. This procedure was repeated three times until the U value (i.e., 6.0156 eV) was identical with respect to the previous iteration.

The geometry obtained from this workflow was then used as input for our phonon calculations at the  $\Gamma$ -point using density functional perturbation theory to compute the Infrared (IR) and Raman spectra of rozenite. The formalism of phonon calculations at the DFT+U level of theory as implemented in Quantum ESPRESSO's ph.x code is presented in detail in Floris et al. (2011, 2020). The open-source Quantum ESPRESSO code suite (Giannozzi et al. 2009, 2017) was used for all ab initio calculations. All files necessary to reproduce our calculations (i.e., input, output, and pseudopotential files) may be accessed on the MaterialsCloudArchive (Meusburger et al. 2022).

#### RESULTS AND DISCUSSION

### 

The crystal structure of rozenite was first determined by Baur (1962) and consists of isolated cyclic  $[Fe(H_2O)_4SO_4]_2$  units (Fig. 2a) interconnected by a hydrogen bond network (Fig. 2b).  $[Fe(H_2O)_4SO_4]_2$  may be further divided into  $Fe(H_2O)_4O_2$  octahedral units that engage in corner-sharing of O atoms with the  $SO_4$  tetrahedral units (Fig. 2a).

Considering that the crystal structure of rozenite has not been revisited since its initial determination 60 years ago by means of single-crystal X-ray diffraction, the results presented in this study improve the literature data substantially. In contrast to X-ray diffraction, which severely underestimates O-H bond lengths (Baur 1972), neutron diffraction is particularly well suited to accurately locate the H atom positions, allowing us to resolve long-standing

ambiguities in the hydrogen bonding network of rozenite. In the following section, the geometry of the octahedral and tetrahedral units will be discussed and compared to the structure reported by Baur (1962) (Table 2).

Overall, the heavy atom (i.e., Fe, S, O) structure refined from the 290 K data set is in excellent agreement with the structure reported by Baur (1962). This is reflected by the mean unsigned differences (MUD)<sup>2</sup> of 0.011 Å (Fe-O bonds), 0.605° (O-Fe-O angles), 0.016 Å (S-O bonds), and (O-S-O angles) 0.76° being either well below or very close to the estimated standard deviations reported by Baur (1962) on the respective quantities.

Moving on to the hydrogen-bond network it is noteworthy that Baur (1962) determined the heavy atom structure of rozenite and did not refine the position of the H atoms. Instead, he fixed the H atoms to the positions determined for the isotypic material MgSO<sub>4</sub>·4H<sub>2</sub>O (starkeyite) during the refinement process. As noted above, Baur (1962) determined the H atom positions by means of X-ray diffraction, which typically yields underestimated bond lengths as well as inaccurate H-O-H angles (Baur 1972). Baur (1962) counteracted this shortcoming by setting multiple constraints upon the hydrogen bond geometries. Therefore, we present for the first time the complete crystal structure of rozenite with all atomic positions derived from an unconstrained refinement. We assess the differences in the hydrogen bonding network and compare our results to the Baur (1962) study (Table 3).

The O···O contacts are in excellent agreement [MUD = 0.0168 Å, largest individual difference (LID) = 0.043 Å], which was expected since the distance of donor acceptor oxygens of the hydrogen bonding network is solely determined by the heavy atom positions. Despite the fact that X-ray diffraction (XRD) underestimates O-H bond lengths, the covalent O-H bond distances in our neutron diffraction and the Baur (1962) XRD study agree very well (MUD = 0.020 Å, LID = 0.063 Å). The reason for this is likely that the bond-length constraints for O-H bonds as applied by Baur (1962) are very close to the values we observed in rozenite. Although the constraints used by Baur (1962) yielded H-O distances in close agreement with our refinement, the constrained model fails for the geometry of the H-O-H molecules, as reflected by a large MUD of 1.05° and LID of 1.80°. Moreover, the H···O

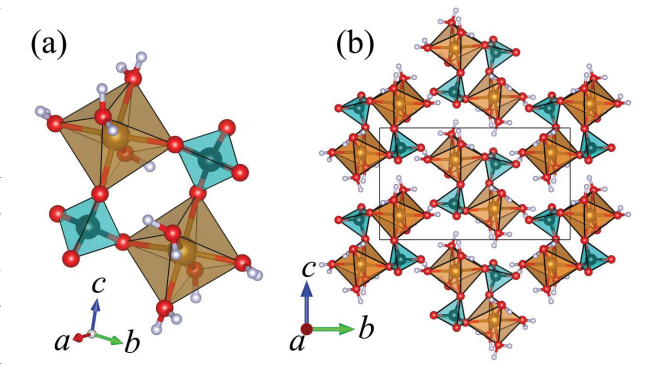


FIGURE 2. Crystal structure of rozenite drawn using the VESTA software (Momma and Izumi 2011). (a) Detailed view of the [Fe(H<sub>2</sub>O)<sub>4</sub>SO<sub>4</sub>]<sub>2</sub> units. Note that the non-hydrated oxygens of the Fe(H<sub>2</sub>O)<sub>4</sub>O<sub>2</sub> units form bridges to the SO<sub>4</sub> tetrahedra (orange and cyan, respectively). (b) The [Fe(H<sub>2</sub>O)<sub>4</sub>SO<sub>4</sub>]<sub>2</sub> isolated units are linked via a complex network of intermolecular hydrogen bonds. (Color online.)

**TABLE 2.** Bond lengths and angles for the octahedral and tetrahedral units as determined in this study at 290 and 21 K and compared to the values reported by Baur (1962)

par	ed to the vai	ues reported		•	
Source	Baur (1962)	This study	Diffa	This study	Diff⁵
T (K)	RT	290		21	
Fe-O1	2.120(9)	2.121(3) -0.001 2.130(3		2.130(3)	-0.009
Fe-O2	2.120(9)	2.130(3)			0.003
Fe-Ow1	2.099(11)	2.096(3)	0.003	2.108(3)	-0.011
Fe-Ow2	2.129(11)	2.139(4)	-0.010	2.145(3)	-0.006
Fe-Ow3	2.127(11)	2.114(4)	0.013 2.113(3)		-0.001
Fe-Ow4	2.126(11)	2.097(3)	0.029	2.094(3)	0.003
MSiD <sup>c</sup>			0.004		-0.003
MUD			0.011		0.006
O1-Fe-Ow1	86.2(2.4)	87.44(11)	-1.24	87.44(10)	0.00
O1-Fe-Ow2	95.7(2.4)	95.51(12)	0.19	95.50(11)	0.01
O1-Fe-Ow3	87.0(2.4)	87.13(12)	-0.13	86.88(10)	0.25
O1-Fe-O2	91.9(2.4)	91.00(10)	0.90	90.81(10)	0.19
Ow4-Fe-Ow1	85.5(2.4)	84.73(12)	0.77	84.36(11)	0.37
Ow4-Fe-Ow2	92.5(2.4)	92.31(13)	0.19	92.69(12)	-0.38
Ow4-Fe-Ow3	92.5(2.4)	92.64(13)	-0.14	92.86(11)	-0.22
Ow4-Fe-O2	88.8(2.4)	89.17(12)	-0.37		
Ow1-Fe-Ow3	90.7(2.4)	4) 91.97(13) -1.2		92.47(11)	-0.50
Ow2-Fe-O2	94.0(2.4)	93.10(12)	93.10(12) 0.90 93.33		-0.23
Ow2-Fe-Ow3	86.8(2.4)	86.8(2.4) 87.35(13) -0.55 86.56(11)		86.56(11)	0.79
MSiD			-0.068		-0.003
MUD			0.605		0.295
S-O1	1.512(8)	1.487(5)	0.025	1.478(5)	0.009
S-O2	1.492(8)	1.482(5)	0.010	1.485(5)	-0.003
S-O3	1.488(8)	1.468(5)	0.002	1.484(5)	-0.016
S-O4	1.473(8)	1.481(5)	-0.008	1.481(6)	0.000
MSiD			0.012		-0.003
MUD			0.016		0.007
O1-S-O2	109.4(1.1)	108.2(3)	1.2	109.7(4)	-1.5
O1-S-O3	108.3(1.1)	110.4(3)	-2.1	109.9(3)	0.5
O1-S-O4	108.3(1.1)	108.7(3)	-0.4	109.0(3)	-0.3
O2-S-O3	109.7(1.1)	109.3(3)	0.4	108.3(3)	1.0
O2-S-O4	111.8(1.1)	111.2(3)	0.6	111.0(3)	0.2
O3-S-O4	109.3(1.1)	109.0(3)	0.3	108.9(4)	0.1
MSiD			-0.24		0.3
MUD			0.76		0.42

<sup>&</sup>lt;sup>a</sup> Refers to the difference between Baur (1962) and this study's 290 K structure. <sup>b</sup> Refers to the difference of this study's 290 and 21 K structures, thus elucidating the influence of temperature on the respective quantity.

$$\frac{\sum_{i}^{n} x_{\rm B} - x_{\rm T}}{n}$$

with  $x_B$  and  $x_T$  being the values as observed by Baur (1962) and in this study, respectively for the quantities of interest (i.e., bond-length and angle).

contacts revealed a LID of 0.209 Å. This failure to accurately describe the hydrogen bonding geometry is most pronounced in the O<sub>w</sub>-H···O angles which exhibit a MUD of 9.51° and LID of up to 30.80°, reinforcing the importance of neutron diffraction data to derive accurate geometries for the complete crystal structure.

The hydrogen bonding system in rozenite-type compounds has been subject of intensive discussions (Baur 1962, 1964, 2002; Kellersohn 1992; Held and Bohaty 2002; Anderson et al. 2012). Based on a long donor acceptor distance of 3.02 Å Baur (1962) suggested that no intermolecular hydrogen bonding takes place for the Ow2-H2b···O2 contact (Fig. 3a). More recent studies on the rozenite-type compounds ZnSO<sub>4</sub>·4D<sub>2</sub>O (Anderson et al. 2012), MnSO<sub>4</sub>·4D<sub>2</sub>O (Held and Bohaty 2002; Anderson et al. 2012), and CoSO<sub>4</sub>·4D<sub>2</sub>O (Kellersohn 1992) interpret H2b to partake in a three-centered interaction (i.e., a bifurcated H-bond, Ow2-H2b :::O2/O2') with long donor-acceptor distances of 3.02 and 3.26 Å (Fig. 3b). Kellersohn (1992) investigated the Ow2 hydrogen bond system based on bond-valance considerations and noted that exclusion of the two long hydrogen bonds results in the O2 atom exhibiting a deficiency of 0.22 valence units. Our own

bond valance calculations (Brown and Altermatt 1985; Brese and O'Keeffe 1991; Alig et al. 1994) for rozenite (Online Materials¹ Table S1) yield a deficiency of 0.10 valence units on the O2 atom, reducing to 0.054 if the intermolecular contacts are included in the calculations. Clearly, the long intermolecular hydrogen bonds play a vital role in achieving charge neutrality for the O2 atom and thus should not be neglected when describing the hydrogen bond network. Supporting this evidence in favor of a three-

**TABLE 3.** Geometry of the hydrogen bonds as determined in this study at 290 and 21 K, and compared to the values reported by Baur (1962)

T(K)         RT         290         21           Ow1-H1a         1.010(8)         0.947(5)         0.063         0.965(5)         −0.018           Ow1-H1b         0.962(9)         0.962(4)         0.000         0.972(4)         −0.01           Ow2-H2b         0.938(9)         0.944(5)         0.014         0.975(4)         −0.01           Ow3-H3a         0.955(8)         0.950(5)         0.005         0.949(4)         −0.01           Ow4-H4b         0.960(8)         0.953(5)         0.007         0.968(4)         −0.015           Ow4-H4b         0.964(9)         0.973(4)         −0.009         0.960(4)         −0.015           Ow4-H4b         0.964(9)         0.973(4)         −0.009         0.960(4)         −0.013           MUD         0.020         0.010         −0.009         0.014         +180           H2a-Ow2-H2b         104.0(8)         105.5(5)         −1.50         107.1(4)         −1.6           H3a-Ow3-H3b         110.2(8)         108.4(4)         1.80         108.1(4)         −3.3           H4a-Ow4-H4b         105.1(8)         105.0(4)         -0.10         106.9(4)         −1.9           MUD         0.01         10.5(8)         1.2	Source	Baur (1962)	This study Diffa This stud		This study	Diff⁵
Ow1-H1b         0.962(9)         0.962(3)         0.000         0.972(4)         -0.01           Ow2-H2b         0.938(9)         0.944(5)         -0.03         0.955(4)         -0.031           Ow3-H3b         0.955(8)         0.954(5)         -0.032         0.952(4)         -0.001           Ow3-H3b         0.957(9)         0.934(4)         -0.003         0.966(4)         -0.015           Ow4-H4a         0.964(9)         0.973(4)         -0.009         0.960(4)         -0.015           Ow4-H4b         0.964(9)         0.973(4)         -0.009         0.960(4)         -0.015           MUD         0.010         0.020         0.014           H1a-Ow1-H1b         105.2(8)         106.0(4)         -0.80         107.1(4)         -1.6           H3a-Ow3-H3b         110.2(8)         108.4(4)         1.80         108.1(4)         -3.           H3a-Ow3-H3b         110.5(8)         105.5(5)         -1.50         107.1(4)         -1.6           H3a-Ow4-H4b         105.1(8)         105.0(4)         1.10         106.9 (4)         -1.90           MSID         M         -0.01         1.05         1.00         1.02         1.40         0.02           Ow1-O3'	<i>T</i> (K)	RT	290		21	
Ow1-H1b         0.962(9)         0.962(4)         0.000         0.972(4)         -0.01           Ow2-H2b         0.933(9)         0.963(5)         -0.03         0.959(4)         0.004           Ow3-H3b         0.955(8)         0.954(5)         0.005         0.949(4)         0.001           Ow3-H3b         0.955(8)         0.953(5)         0.007         0.968(4)         -0.015           Ow4-H4a         0.960(8)         0.953(5)         0.007         0.968(4)         -0.015           Ow4-H4b         0.964(9)         0.973(4)         -0.009         0.960(4)         -0.015           MUD         0.020         0.014         -0.009         0.020         0.014           H1a-Ow1-H1b         105.2(8)         106.0(4)         -0.80         107.8(4)         -1.80           H2a-Ow2-H2b         104.0(8)         105.5(5)         -1.50         107.1(4)         -1.6           H3a-Ow3-H3b         110.2(8)         106.0(4)         1.80         108.1(4)         0.3           H3a-Ow4-H4b         105.1(8)         105.0(4)         1.10         106.9 (4)         -1.90           MSiD         0.01-03'         2.857(10)         2.898(4)         -0.04         2.84(4)         0.02	Ow1-H1a	1.010(8)	0.947(5)	0.063	0.965(5)	-0.018
Ow2-H2a         0,933(9)         0,963(5)         -0.03         0,959(4)         -0.004           Ow2-H2b         0,958(8)         0,950(5)         0.005         0,949(4)         -0.001           Ow3-H3b         0,955(8)         0,950(5)         0.005         0,949(4)         -0.019           Ow4-H4b         0,960(8)         0,953(5)         0.007         0,968(4)         -0.019           MWLD         0,964(9)         0,973(4)         -0.009         0,960(4)         -0.013           MSID         0,010         0,010         0,014           H1a-Ow1-H1b         105.2(8)         106.0(4)         -0.80         107.8(4)         -1.80           H2a-Ow2-H2b         104.0(8)         105.5(5)         -1.50         107.1(4)         -1.6           H3a-Ow3-H31b         110.2(8)         108.4(4)         1.80         108.1(4)         0.3           H4a-Ow4-H4b         105.1(8)         105.0(4)         0.10         106.9 (4)         -1.90           MSID         105.2         2.898(4)         -0.043         2.848(4)         0.03           Ow1-03         2.285(10)         2.898(4)         -0.042         2.844(4)         0.050           Ow2-02         3.023(10)         3.0						
Ow2-H2b         0.958(9)         0.944(5)         0.014         0.975(4)         -0.031           Ow3-H3a         0.955(8)         0.950(5)         0.005         0.095(4)         -0.019           Ow4-H4a         0.960(8)         0.953(5)         0.007         0.968(4)         -0.015           Ow4-H4b         0.964(9)         0.973(4)         -0.009         0.960(4)         -0.015           MUD         0.020         0.010         -0.009           MUD         0.020         0.014         -1.80           H1a-Ow1-H1b         105.2(8)         106.0(4)         -0.80         107.8(4)         -1.80           H2a-Ow2-H2b         104.0(8)         105.5(5)         -1.50         107.1(4)         -1.6           H3a-Ow3-H3b         110.2(8)         108.4(4)         1.80         108.1(4)         0.3           H4a-Ow4-H4b         105.1(8)         105.0(4)         -0.10         106.9 (4)         -1.90           MSiD         -0.01         1.05         -0.10         106.9 (4)         -1.90           MV1-O3         2.855(10)         2.898(4)         -0.043         2.848(4)         0.05           Ow1-O3'         2.850(10)         2.898(4)         -0.002         2.244(4)	Ow2-H2a		. ,			
Ow3-H3b         0.955(8)         0.950(5)         0.005         0.949(4)         0.001           Ow3-H3b         0.975(9)         0.943(4)         0.032         0.962(4)         -0.015           Ow4-H4b         0.960(8)         0.953(5)         0.007         0.968(4)         -0.013           MSID         0.010         0.010         0.014           H1a-Ow1-H1b         105.2(8)         106.0(4)         -0.80         107.8(4)         -1.80           H2a-Ow2-H2b         104.0(8)         105.5(5)         -1.50         107.1(4)         -1.6           H3a-Ow3-H3b         110.2(8)         108.4(4)         1.80         108.1(4)         0.3           H4a-Ow4-H4b         105.1(8)         105.0(4)         -0.10         10.5         -1.5           MUD         1.05         -0.10         -1.25         1.40           Ow1-03         2.855(10)         2.898(4)         -0.043         2.848(4)         0.050           Ow1-03         2.857(10)         2.764(4)         0.026         2.744(4)         0.020           Ow2-04         2.867(10)         2.885(4)         0.009         2.834(4)         0.024           Ow2-02         3.267(10         3.274(4)         -0.007			. ,		, ,	
Ow3-H3b Ow4-H4a         0.975(9) 0.960(8)         0.934(4) 0.953(5)         0.032 0.007         0.962(4) 0.968(4)         -0.019 0.093(4)         -0.019 0.060(4)         -0.019 0.060(4)         -0.019 0.060(4)         -0.019 0.020         -0.009 0.000         -0.009 0.010         -0.009 0.010         -0.009 0.010         -0.009 0.010         -0.009 0.010         -0.009 0.010         -0.009 0.010         -0.009 0.010         -0.009 0.014         -1.50 0.014         -1.50 0.017,1(4)         -1.60 -1.6         -1.50 0.017,1(4)         -1.6         -1.50 0.017,1(4)         -1.6         -1.50 0.017,1(4)         -1.6         -1.50 0.010         -0.010 0.010         -1.05 0.010         -1.05 0.010         -1.25 0.010         -1.25 0.010         -1.05 0.010         -1.25 0.050         -1.25 0.050         -1.05 0.010         -1.05 0.010         -1.25 0.050         -1.25 0.050         -1.05 0.010         -1.25 0.050         -1.25 0.050         -1.05 0.050         -1.25 0.050         -1.05 0.050         -1.25 0.050         -1.05 0.050         -1.25 0.050         -1.05 0.050         -1.25 0.050         -1.05 0.050         -1.25 0.050         -1.						
Owa-H-Hab         0.960(8)         0.953(5)         0.007         0.968(4)         -0.015           Owa-H-Hab         0.964(9)         0.973(4)         -0.009         0.960(4)         0.013           MSID         0.010         0.020         0.014           H1a-Ow1-H1b         105.2(8)         106.0(4)         -0.80         107.1(4)         -1.60           H2a-Ow2-H2b         104.0(8)         105.5(5)         -1.50         107.1(4)         -1.6           H3a-Ow3-H3b         110.2(8)         108.4(4)         1.80         108.1(4)         0.3           H4a-Ow4-H4b         105.1(8)         105.0(4)         0.10         106.9(4)         -1.90           MUD         1.05         1.05         1.40         1.05         1.40           Ow1-03'         2.895(10)         2.888(4)         -0.043         2.844(4)         0.050           Ow1-03'         2.790(10)         2.764(4)         0.026         2.744(4)         0.020           Ow2-04         2.867(10)         2.888(4)         -0.009         2.834(4)         0.024           Ow2-02'         3.025(10)         3.215(4)         -0.009         2.794(4)         0.024           Ow3-04         2.845(10)         2.836(4)<			. ,			
Owa-Habb         0.964(9)         0.973(4)         -0.009         0.960(4)         0.010           MSID         0.010         -0.009           MUD         105.2(8)         106.0(4)         -0.80         107.8(4)         -1.80           H2a-Ow2-H2b         104.0(8)         105.5(5)         -1.50         107.1(4)         -1.6           H3a-Ow3-H3b         110.2(8)         108.4(4)         1.80         108.1(4)         0.3           H4a-Ow4-H4b         105.1(8)         105.0(4)         0.10         106.9(4)         -1.90           MSID         -0.10         1.05         -1.25         MUD         -0.10         1.40           Ow1-03'         2.790(10)         2.764(4)         0.026         2.744(4)         0.020           Ow2-04         2.867(10)         2.858(4)         -0.043         2.848(4)         0.020           Ow2-02'         3.023(10)         3.015(4)         0.009         2.834(4)         0.020           Ow2-02'         3.267(10         3.274(4)         -0.007         3.250(4)         0.024           Ow3-01         2.805(10)         2.836(4)         -0.007         3.250(4)         0.022           Ow3-04         2.805(10)         2.848(4)			. ,			
MSID		, ,	. ,		, ,	
MUD						
H1a-Ow1-H1b   105.2(8)						
H22-Ow2-H2b		105.2(8)	106.0(4)		107.8(4)	
H3a-Ow3-H3b						
H4a-Ow4-H4b   105.1(8)   105.0(4)   0.10   106.9 (4)   -1.90   MSiD   -0.10   -1.25   1.40   Ow1-O3   2.855(10)   2.898(4)   -0.043   2.848(4)   0.050   Ow1-O3   2.790(10)   2.764(4)   0.026   2.744(4)   0.020   Ow2-O4   2.867(10)   2.858(4)   0.009   2.834(4)   0.020   Ow2-O2   3.023(10)   3.015(4)   0.008   2.986(4)   0.029   Ow2-O2   3.267(10   3.274(4)   -0.007   3.250(4)   0.024   Ow3-O4   2.845(10)   2.836(4)   0.009   2.794(4)   0.024   Ow3-O4   2.845(10)   2.836(4)   0.009   2.794(4)   0.030   Ow3-O4   2.845(10)   2.816(4)   -0.011   2.795(4)   0.031   Ow3-O4   2.837(10)   2.816(4)   -0.011   2.795(4)   0.021   Ow4-O4   2.837(10)   2.733(4)   -0.010   2.718(4)   0.016   Ow4-O3   2.723(10)   2.733(4)   -0.010   2.718(4)   0.015   Ow4-O3   2.723(10)   2.733(4)   -0.010   2.718(4)   0.015   Ow1-O32   H1a-O3   1.865(6)   1.957(4)   -0.092   1.888(4)   0.026   H1b-O3'   1.834(6)   1.892(5)   0.209   1.967(4)   0.032   H2a-O4   2.201(6)   1.992(5)   0.209   1.967(4)   0.025   H2b-O2   2.417(6)   2.330(5)   0.087   2.249(4)   0.081   H2b-O2'   2.593(6)   2.551(4)   0.042   2.525(4)   0.026   H3a-O4   2.113(6)   2.015(4)   0.098   1.974(4)   0.041   H3a-Ow4   2.345(9)   2.425(5)   -0.080   2.399(4)   0.026   H3b-O1   1.833(6)   1.874(4)   -0.041   1.834(6)   0.037   MUD   0.083   0.037   0.041   0.037   0.042   0.050			. ,			
MSID						
MUD         1.05         1.40           Ow1-O3'         2.790(10)         2.764(4)         -0.043         2.848(4)         0.050           Ow1-O3'         2.790(10)         2.764(4)         0.026         2.744(4)         0.020           Ow2-O4         2.867(10)         2.858(4)         0.009         2.834(4)         0.024           Ow2-O2         3.023(10)         3.015(4)         0.008         2.986(4)         0.029           Ow3-O4         2.845(10)         2.836(4)         0.009         2.794(4)         0.04           Ow3-O4         3.025(12)         3.059(5)         -0.034         3.029(4)         0.030           Ow3-O4         2.845(10)         2.816(4)         -0.011         2.795(4)         0.021           Ow4-O4         2.837(10)         2.848(4)         -0.011         2.892(4)         0.016           Ow4-O3         2.723(10)         2.733(4)         -0.010         2.718(4)         0.015           MUD         0.0168         0.027         0.0064         0.027           H1a-O3         1.865(6)         1.957(4)         -0.092         1.884(0)         0.069           H2a-O4         2.201(6)         1.992(5)         0.209         1.967(4)			. 05.0(1)			
Ow1-O3         2.855(10)         2.898(4)         -0.043         2.848(4)         0.020           Ow1-O3'         2.790(10)         2.764(4)         0.026         2.744(4)         0.020           Ow2-O4         2.867(10)         2.858(4)         0.009         2.834(4)         0.024           Ow2-O2'         3.023(10)         3.015(4)         0.008         2.986(4)         0.029           Ow3-O4         2.845(10)         2.836(4)         0.009         2.794(4)         0.042           Ow3-Ow4         3.025(12)         3.059(5)         -0.034         3.029(4)         0.032           Ow3-OH         2.805(10)         2.816(4)         -0.011         2.795(4)         0.021           Ow4-O4         2.837(10)         2.848(4)         -0.011         2.832(4)         0.016           MUD         0.0168         -0.0064         0.027           H1a-O3         1.834(6)         1.957(4)         -0.092         1.884(4)         0.005           H2b-O4         2.201(6)         1.992(5)         0.209         1.967(4)         0.025           H2b-O2         2.417(6)         2.330(5)         0.087         2.249(4)         0.081           H2b-O2         2.417(6)         2.330(5)						
Ow1-O3'         2.790(10)         2.764(4)         0.026         2.744(4)         0.020           Ow2-O4         2.867(10)         2.858(4)         0.009         2.834(4)         0.024           Ow2-O2'         3.023(10)         3.015(4)         0.008         2.986(4)         0.024           Ow2-O2'         3.267(10         3.274(4)         -0.007         3.250(4)         0.024           Ow3-O4         2.845(10)         2.836(4)         0.009         2.794(4)         0.042           Ow3-O4         3.025(12)         3.059(5)         -0.034         3.029(4)         0.030           Ow3-O4         2.805(10)         2.816(4)         -0.011         2.795(4)         0.021           Ow4-O4         2.837(10)         2.848(4)         -0.011         2.732(4)         0.016           MUD         0.0168         0.027         0.027         0.027           MUD         0.0168         0.027         0.027           H1a-O3         1.865(6)         1.957(4)         -0.092         1.888(4)         0.069           H1b-O3'         1.834(6)         1.808(4)         0.026         1.776(4)         0.032           H2a-O4         2.201(6)         1.992(5)         0.209		2.855(10)	2.898(4)		2.848(4)	
Ow2-O4         2.867(10)         2.858(4)         0.009         2.834(4)         0.024           Ow2-O2         3.023(10)         3.015(4)         0.008         2.986(4)         0.029           Ow2-O2'         3.267(10)         3.274(4)         -0.007         3.250(4)         0.029           Ow3-O4         2.845(10)         2.836(4)         0.009         2.794(4)         0.042           Ow3-Ow4         3.025(12)         3.059(5)         -0.034         3.029(4)         0.030           Ow3-Ow4         3.025(12)         3.059(5)         -0.034         3.029(4)         0.030           Ow3-Ow4         2.805(10)         2.816(4)         -0.011         2.795(4)         0.021           Ow4-O4         2.837(10)         2.848(4)         -0.011         2.832(4)         0.016           MSID         -0.0064         0.027         0.016         0.027           MUD         -0.0064         0.027         0.027           H1a-O3         1.855(6)         1.957(4)         -0.092         1.884(4)         0.027           H2a-O4         2.201(6)         1.992(5)         0.209         1.967(4)         0.032           H2b-O2         2.417(6)         2.330(5)         0.087						
Ow2-O2         3.023(10)         3.015(4)         0.008         2.986(4)         0.029           Ow2-O2'         3.267(10)         3.274(4)         -0.007         3.250(4)         0.024           Ow3-O4         2.845(10)         2.836(4)         0.009         2.794(4)         0.042           Ow3-Ow4         3.025(12)         3.059(5)         -0.034         3.029(4)         0.030           Ow3-O1         2.805(10)         2.816(4)         -0.011         2.795(4)         0.021           Ow4-O3         2.723(10)         2.733(4)         -0.010         2.718(4)         0.016           MSID         0.0168         0.027         0.0168         0.027           MUD         0.0168         0.027         0.0168         0.027           H1a-O3         1.865(6)         1.957(4)         -0.092         1.888(4)         0.027           H1b-O3'         1.834(6)         1.808(4)         0.026         1.776(4)         0.032           H2a-O4         2.201(6)         1.992(5)         0.209         1.867(4)         0.025           H2b-O2'         2.439(6)         2.551(4)         0.042         2.525(4)         0.026           H3a-O4         2.113(6)         2.015(4)						
Ow2-O2'         3.267(10         3.274(4)         -0.007         3.250(4)         0.024           Ow3-O4         2.845(10)         2.836(4)         0.009         2.794(4)         0.042           Ow3-Ow4         3.025(12)         3.059(5)         -0.034         3.029(4)         0.030           Ow3-O1         2.805(10)         2.848(4)         -0.011         2.795(4)         0.021           Ow4-O4         2.837(10)         2.848(4)         -0.010         2.718(4)         0.015           MSID         -0.0064         0.027           MUD         0.0168         0.027           H1a-O3         1.865(6)         1.957(4)         -0.092         1.888(4)         0.027           H1b-O3'         1.834(6)         1.808(4)         0.026         1.776(4)         0.025           H2b-O2         2.417(6)         2.330(5)         0.087         2.249(4)         0.081           H2b-O2'         2.593(6)         2.551(4)         0.042         2.552(4)         0.026           H3a-O4         2.113(6)         2.015(4)         0.098         1.974(4)         0.041           H3a-O4         1.833(6)         1.874(4)         -0.041         1.834(4)         0.026		. ,	. ,		, ,	
Ow3-O4         2.845(10)         2.836(4)         0.009         2.794(4)         0.042           Ow3-Ow4         3.025(12)         3.059(5)         -0.034         3.029(4)         0.030           Ow3-O1         2.805(10)         2.816(4)         -0.011         2.795(4)         0.021           Ow4-O4         2.837(10)         2.848(4)         -0.011         2.832(4)         0.016           MUD         0.0168         0.027         0.0168         0.027           H1a-O3         1.865(6)         1.957(4)         -0.092         1.888(4)         0.069           H1b-O3'         1.834(6)         1.808(4)         0.026         1.776(4)         0.032           H2b-O2         2.417(6)         2.330(5)         0.087         2.249(4)         0.081           H2b-O2         2.593(6)         2.551(4)         0.042         2.525(4)         0.026           H3a-O4         2.113(6)         2.015(4)         0.098         1.974(4)         0.041           H3a-O4         1.833(6)         1.874(4)         -0.080         2.399(4)         0.026           H3b-O1         1.833(6)         1.874(4)         -0.081         1.834(4)         0.041           H4a-O4         1.969(6)						
Ow3-Ow4         3.025(12)         3.059(5)         -0.034         3.029(4)         0.030           Ow3-O1         2.805(10)         2.816(4)         -0.011         2.795(4)         0.021           Ow4-O4         2.837(10)         2.848(4)         -0.011         2.795(4)         0.016           Ow4-O3         2.723(10)         2.733(4)         -0.010         2.718(4)         0.015           MSID         -0.0064         0.027           MUD         0.0168         0.027           H1a-O3         1.865(6)         1.957(4)         -0.092         1.888(4)         0.069           H1b-O3'         1.834(6)         1.898(4)         0.026         1.776(4)         0.032           H2a-O4         2.201(6)         1.992(5)         0.209         1.967(4)         0.025           H2b-O2         2.417(6)         2.330(5)         0.087         2.249(4)         0.081           H2b-O2'         2.593(6)         2.551(4)         0.042         2.525(4)         0.026           H3a-O4         2.13(6)         2.015(4)         0.098         1.974(4)         0.041           H3a-O4         1.833(6)         1.874(4)         -0.041         1.834(4)         0.040 <t< td=""><td></td><td></td><td>, ,</td><td></td><td>, ,</td><td></td></t<>			, ,		, ,	
Ow3-O1         2.805(10)         2.816(4)         -0.011         2.795(4)         0.021           Ow4-O4         2.837(10)         2.848(4)         -0.011         2.832(4)         0.016           Ow4-O3         2.723(10)         2.733(4)         -0.010         2.718(4)         0.015           MSID         -0.0064         0.027           MUD         0.0168         0.027           H1a-O3         1.865(6)         1.957(4)         -0.092         1.888(4)         0.069           H1b-O3'         1.834(6)         1.808(4)         0.026         1.776(4)         0.032           H2a-O4         2.201(6)         1.992(5)         0.209         1.967(4)         0.025           H2b-O2'         2.417(6)         2.330(5)         0.087         2.249(4)         0.081           H2b-O2'         2.593(6)         2.551(4)         0.042         2.525(4)         0.026           H3a-O4         2.113(6)         2.015(4)         0.098         1.974(4)         0.041           H3a-O4         1.833(6)         1.874(4)         -0.041         1.834(4)         0.041           H3a-O4         1.969(6)         1.948(4)         0.021         1.918(4)         0.037 <th< td=""><td></td><td>. ,</td><td>. ,</td><td></td><td></td><td></td></th<>		. ,	. ,			
Ow4-O4         2.837(10)         2.848(4)         -0.011         2.832(4)         0.016           Ow4-O3         2.723(10)         2.733(4)         -0.010         2.718(4)         0.015           MSID         -0.0064         0.027           MUD         0.0168         0.027           H1a-O3         1.865(6)         1.957(4)         -0.092         1.888(4)         0.069           H1b-O3'         1.834(6)         1.808(4)         0.026         1.776(4)         0.032           H2a-O4         2.201(6)         1.992(5)         0.009         1.967(4)         0.025           H2b-O2         2.417(6)         2.330(5)         0.087         2.249(4)         0.081           H2b-O2'         2.593(6)         2.551(4)         0.042         2.525(4)         0.026           H3a-O4         2.113(6)         2.015(4)         0.098         1.974(4)         0.041           H3a-O4         2.13(6)         2.015(4)         0.098         1.974(4)         0.041           H3b-O1         1.833(6)         1.874(4)         -0.041         1.834(4)         0.041           H4a-O4         1.969(6)         1.948(4)         0.021         1.918(4)         0.093           H4b						
Ow4-O3         2.723(10)         2.733(4)         -0.010         2.718(4)         0.015           MSID         -0.0064         0.027           MUD         0.0168         0.027           H1a-O3         1.865(6)         1.957(4)         -0.092         1.888(4)         0.069           H1b-O3'         1.834(6)         1.808(4)         0.026         1.776(4)         0.032           H2a-O4         2.201(6)         1.992(5)         0.209         1.967(4)         0.025           H2b-O2         2.417(6)         2.330(5)         0.087         2.249(4)         0.081           H2b-O2'         2.593(6)         2.551(4)         0.042         2.525(4)         0.026           H3a-O4         2.113(6)         2.015(4)         0.098         1.974(4)         0.041           H3a-O4         2.1345(9)         2.425(5)         -0.080         2.399(4)         0.026           H3b-O1         1.833(6)         1.874(4)         -0.041         1.834(4)         0.040           H4a-O4         1.969(6)         1.948(4)         0.021         1.918(4)         0.093           MUD         0.031         0.041         0.037           MUD         0.032         0.041						
MSID MUD         —0.0064 0.0168         —0.027 0.0168           H1a-O3         1.865(6)         1.957(4)         —0.092         1.888(4)         0.069           H1b-O3'         1.834(6)         1.808(4)         —0.026         1.776(4)         —0.032           H2a-O4         2.201(6)         1.992(5)         0.209         1.967(4)         —0.025           H2b-O2         2.417(6)         2.330(5)         0.087         2.249(4)         0.081           H2b-O2'         2.593(6)         2.551(4)         0.042         2.525(4)         0.026           H3a-O4         2.113(6)         2.015(4)         0.098         1.974(4)         0.041           H3a-O4         2.134(6)         2.015(4)         0.098         2.399(4)         0.026           H3b-O1         1.833(6)         1.874(4)         —0.080         2.399(4)         0.026           H3b-O3         1.899(6)         1.948(4)         0.021         1.918(4)         0.093           H4b-O3         1.899(6)         1.764(4)         0.135         1.764(4)         0.037           MUD         0.083         0.037         0.041         0.037         0.041         0.037           MUD         0.084-Ow2-O2         144.5(4)<			: ::			
MUD         0.0168         0.027           H1a-O3         1.865(6)         1.957(4)         -0.092         1.888(4)         0.069           H1b-O3'         1.834(6)         1.808(4)         0.026         1.776(4)         0.032           H2a-O4         2.201(6)         1.992(5)         0.209         1.967(4)         0.025           H2b-O2         2.417(6)         2.330(5)         0.087         2.249(4)         0.081           H2b-O2'         2.593(6)         2.551(4)         0.042         2.525(4)         0.026           H3a-O4         2.113(6)         2.015(4)         0.098         1.974(4)         0.041           H3a-Ow4         2.345(9)         2.425(5)         -0.080         2.399(4)         0.026           H3b-O1         1.833(6)         1.874(4)         -0.041         1.834(4)         0.040           H4a-O4         1.969(6)         1.948(4)         0.021         1.918(4)         0.093           H4b-O3         1.899(6)         1.764(4)         0.135         1.764(4)         0.000           MSID         0.081         0.083         0.037           MUD         0.083         0.037         0.037         0.044         0.40-0w2-02'         92.6(3)		(,	( .,		( . ,	
H1a-O3						
H1b-O3'   1.834(6)   1.808(4)   0.026   1.776(4)   0.032   H2a-O4   2.201(6)   1.992(5)   0.209   1.967(4)   0.025   H2b-O2   2.417(6)   2.330(5)   0.087   2.249(4)   0.081   H2b-O2'   2.593(6)   2.551(4)   0.042   2.525(4)   0.026   H3a-O4   2.113(6)   2.015(4)   0.098   1.974(4)   0.041   H3a-Ow4   2.345(9)   2.425(5)   -0.080   2.399(4)   0.026   H3b-O1   1.833(6)   1.874(4)   -0.041   1.834(4)   0.040   H4a-O4   1.969(6)   1.948(4)   0.021   1.918(4)   0.093   H4b-O3   1.899(6)   1.764(4)   0.135   1.764(4)   0.037   MUD   0.081   0.081   0.081   0.037   0.080   0.080   0.037   0.080		1.865(6)	1.957(4)		1.888(4)	
H2a-O4						
H2b-O2						
H2b-O2'   2.593(6)   2.551(4)   0.042   2.525(4)   0.026   H3a-O4   2.113(6)   2.015(4)   0.098   1.974(4)   0.041   H3a-Ow4   2.345(9)   2.425(5)   -0.080   2.399(4)   0.026   H3b-O1   1.833(6)   1.874(4)   -0.041   1.834(4)   0.040   H4a-O4   1.969(6)   1.948(4)   0.021   1.918(4)   0.093   H4b-O3   1.899(6)   1.764(4)   0.135   1.764(4)   0.000   MSiD   0.041   0.037   0.083   0.037   0.083   0.037   0.083   0.037   0.083   0.037   0.080   0.080	H2b-O2		2.330(5)	0.087		0.081
H3a-O4         2.113(6)         2.015(4)         0.098         1.974(4)         0.041           H3a-Ow4         2.345(9)         2.425(5)         -0.080         2.399(4)         0.026           H3b-O1         1.833(6)         1.874(4)         -0.041         1.834(4)         0.040           H4a-O4         1.969(6)         1.948(4)         0.021         1.918(4)         0.093           H4b-O3         1.899(6)         1.764(4)         0.135         1.764(4)         0.037           MUD         0.081         0.081         0.037           MUD         0.083         0.037           O3-Ow1-O3'         104.8(4)         104.90 (11)         -0.10         104.46(10)         0.44           O4-Ow2-O2'         144.5(4)         143.43(14)         1.07         142.81(12)         0.62           O4-Ow3-O1         137.2(4)         136.23(13)         0.97         135.54(11)         0.69           Ow4-Ow3-O1         70.8(3)         70.28(10)         0.52         69.45(8)         0.83           O4-Ow4-O3         117.3(4)         116.68(12)         0.62         118.30(11)         -1.62           MSiD         0.43         0.43         0.055           MUD <td< td=""><td>H2b-O2'</td><td>2.593(6)</td><td>2.551(4)</td><td>0.042</td><td>2.525(4)</td><td>0.026</td></td<>	H2b-O2'	2.593(6)	2.551(4)	0.042	2.525(4)	0.026
H3b-O1         1.833(6)         1.874(4)         -0.041         1.834(4)         0.040           H4a-O4         1.969(6)         1.948(4)         0.021         1.918(4)         0.093           H4b-O3         1.899(6)         1.764(4)         0.135         1.764(4)         0.000           MSiD         0.041         0.037         0.037         0.0037         0.0037         0.0037           MUD         0.083         0.037         0.037         0.0037         0.0037         0.0037           O3-Ow1-O3'         104.8(4)         104.90 (11)         -0.10         104.46(10)         0.44           O4-Ow2-O2         144.5(4)         143.43(14)         1.07         142.81(12)         0.62           O4-Ow3-O1         137.2(4)         136.23(13)         0.97         135.54(11)         0.69           Ow4-Ow3-O1         70.8(3)         70.28(10)         0.52         69.45(8)         0.83           O4-Ow4-O3         117.3(4)         116.68(12)         0.62         118.30(11)         -1.62           MSiD         0.43         0.055         0.83         0.055           MUD         0.63         0.805         0.83           OW1-H1a-O3         165.8(5)         172.0	H3a-O4		2.015(4)	0.098	1.974(4)	0.041
H4a-O4         1.969(6)         1.948(4)         0.021         1.918(4)         0.093           H4b-O3         1.899(6)         1.764(4)         0.135         1.764(4)         0.000           MSiD         0.041         0.037         0.037         0.037           MUD         0.083         0.037         0.037           O3-Ow1-O3'         104.8(4)         104.90 (11)         -0.10         104.46(10)         0.44           O4-Ow2-O2'         92.6(3)         93.12(11)         -0.52         93.75(9)         -0.63           O4-Ow3-O1         137.2(4)         136.23(13)         0.97         135.54(11)         0.69           Ow4-Ow3-O1         70.8(3)         70.28(10)         0.52         69.45(8)         0.83           O4-Ow4-O3         117.3(4)         116.68(12)         0.62         118.30(11)         -1.62           MSiD         0.43         0.055         0.805           MUD         0.63         0.805           Ow1-H1a-O3         165.8(5)         172.0(4)         -6.2         173.5(4)         -1.60           Ow2-H2a-O4         125.7(6)         148.5(4)         -22.8         149.2(3)         -0.70           Ow2-H2b-O2'         129.6(6)         <	H3a-Ow4	2.345(9)	2.425(5)	-0.080	2.399(4)	0.026
H4b-O3         1.899(6)         1.764(4)         0.135         1.764(4)         0.000           MSiD         0.041         0.037           MUD         0.083         0.037           O3-Ow1-O3'         104.8(4)         104.90 (11)         -0.10         104.46(10)         0.44           O4-Ow2-O2'         144.5(4)         143.43(14)         1.07         142.81(12)         0.62           O4-Ow2-O2'         92.6(3)         93.12(11)         -0.52         93.75(9)         -0.63           O4-Ow3-O1         137.2(4)         136.23(13)         0.97         135.54(11)         0.69           Ow4-Ow3-O1         70.8(3)         70.28(10)         0.52         69.45(8)         0.83           O4-Ow4-O3         117.3(4)         116.68(12)         0.62         118.30(11)         -1.62           MSID         0.43         0.055         0.805         0.805           MUD         0.62         173.5(4)         -1.60           Ow1-H1a-O3'         165.8(5)         172.0(4)         -6.2         173.5(4)         -1.60           Ow2-H2a-O4         125.7(6)         148.5(4)         -22.8         149.2(3)         -0.70           Ow2-H2b-O2'         129.6(6)         129.0(4) </td <td>H3b-O1</td> <td>1.833(6)</td> <td>1.874(4)</td> <td>-0.041</td> <td>1.834(4)</td> <td>0.040</td>	H3b-O1	1.833(6)	1.874(4)	-0.041	1.834(4)	0.040
MSiD MUD         0.041 0.083         0.037 0.037           O3-Ow1-O3'         104.8(4)         104.90 (11)         -0.10         104.46(10)         0.44           O4-Ow2-O2         144.5(4)         143.43(14)         1.07         142.81(12)         0.62           O4-Ow2-O2'         92.6(3)         93.12(11)         -0.52         93.75(9)         -0.63           O4-Ow3-O1         137.2(4)         136.23(13)         0.97         135.54(11)         0.69           Ow4-Ow3-O1         70.8(3)         70.28(10)         0.52         69.45(8)         0.83           O4-Ow4-O3         117.3(4)         116.68(12)         0.62         118.30(11)         -1.62           MSiD         0.43         0.055         MUD         0.63         0.805           OW1-H1a-O3         165.8(5)         172.0(4)         -6.2         173.5(4)         -1.60           Ow1-H2a-O4         125.7(6)         148.5(4)         -22.8         149.2(3)         -0.70           Ow2-H2b-O2         122.6(6)         129.0(4)         -6.4         131.0(3)         2.60           Ow3-H3a-O4         132.3(6)         143.6(3)         -11.3         143.4(3)         0.20           Ow3-H3b-O1         173.7(5)         17	H4a-O4	1.969(6)	1.948(4)	0.021	1.918(4)	0.093
MUD         0.083         0.037           O3-Ow1-O3'         104.8(4)         104.90 (11)         -0.10         104.46(10)         0.44           O4-Ow2-O2         144.5(4)         143.43(14)         1.07         142.81(12)         0.62           O4-Ow2-O2'         92.6(3)         93.12(11)         -0.52         93.75(9)         -0.63           O4-Ow3-O1         137.2(4)         136.23(13)         0.97         135.54(11)         0.69           Ow4-Ow3-O1         70.8(3)         70.28(10)         0.52         69.45(8)         0.83           O4-Ow4-O3         117.3(4)         116.68(12)         0.62         118.30(11)         -1.62           MSiD         0.43         0.055           MUD         0.63         0.805           Ow1-H1a-O3         165.8(5)         172.0(4)         -6.2         173.5(4)         -1.60           Ow1-H2a-O4         125.7(6)         148.5(4)         -22.8         149.2(3)         -0.70           Ow2-H2b-O2         122.6(6)         129.0(4)         -6.4         131.0(3)         2.60           Ow3-H3a-O4         132.3(6)         143.6(3)         -11.3         143.4(3)         0.20           Ow3-H3b-O1         173.7(5)	H4b-O3	1.899(6)	1.764(4)	0.135	1.764(4)	0.000
O3-Ow1-O3'         104.8(4)         104.90 (11)         -0.10         104.46(10)         0.44           O4-Ow2-O2         144.5(4)         143.43(14)         1.07         142.81(12)         0.62           O4-Ow2-O2'         92.6(3)         93.12(11)         -0.52         93.75(9)         -0.63           O4-Ow3-O1         137.2(4)         136.23(13)         0.97         135.54(11)         0.69           Ow4-Ow3-O1         70.8(3)         70.28(10)         0.52         69.45(8)         0.83           O4-Ow4-O3         117.3(4)         116.68(12)         0.62         118.30(11)         -1.62           MSiD         0.43         0.055         0.805           MUD         0.63         0.805           Ow1-H1a-O3         165.8(5)         172.0(4)         -6.2         173.5(4)         -1.60           Ow2-H2a-O4         125.7(6)         148.5(4)         -22.8         149.2(3)         -0.70           Ow2-H2b-O2         122.6(6)         129.0(4)         -6.4         131.5(3)         -2.50           Ow3-H3a-O4         132.3(6)         143.6(3)         -11.3         143.4(3)         0.20           Ow3-H3a-Ov4         127.7(6)         124.0(3)         3.7         123.6(3)	MSiD			0.041		0.037
O4-Ow2-O2 O4-Ow2-O2'         144.5(4) 92.6(3)         143.43(14) 93.12(11)         1.07 -0.52         142.81(12) 93.75(9)         0.62 -0.63           O4-Ow3-O1 Ow4-Ow3-O1         137.2(4) 70.8(3)         136.23(13) 70.28(10)         0.52 0.52         69.45(8) 69.45(8)         0.83 0.80           O4-Ow4-O3 MSID         117.3(4) 116.68(12)         0.62 0.63 0.80         118.30(11) 0.63 0.805         -1.62 0.805           Ow1-H1a-O3 0w1-H1b-O3'         165.8(5) 171.8(6) 172.5(4)         172.5(4) -0.7         -0.7 173.1(4) -0.60         -0.60 0w2-H2a-O4 0w2-H2b-O2'         122.6(6) 129.0(4) 129.0(4) -6.4         131.5(3) 131.6(3) -0.20         -0.70 0w2-H2b-O2'         129.6(6) 129.6(6) 133.6(4) -4.0         131.0(3) 130.0(3) 2.60 0w3-H3a-O4 127.7(6) 124.0(3) 3.7         123.6(3) 143.4(3) 0.20 0w3-H3b-O1 173.7(5) 175.4(4) -1.7         176.0(3) -0.60 0w4-H4a-O4 149.2(6) 156.7(4) -7.5 156.4(3) 0.30 0w4-H4b-O3 141.8(5) 172.6(4) -30.8 172.2(3) 0.40 0w3-H3b-O1 0w4-H4b-O3 141.8(5) 172.6(4) -30.8 172.2(3) 0.40 0w3-H3b-O1 0w4-H4b-O3 141.8(5) 0.980	MUD			0.083		0.037
O4-Ow2-O2'         92.6(3)         93.12(11)         -0.52         93.75(9)         -0.63           O4-Ow3-O1         137.2(4)         136.23(13)         0.97         135.54(11)         0.69           Ow4-Ow3-O1         70.8(3)         70.28(10)         0.52         69.45(8)         0.83           O4-Ow4-O3         117.3(4)         116.68(12)         0.62         118.30(11)         -1.62           MSID         0.63         0.805           MUD         0.63         0.805           Ow1-H1a-O3         165.8(5)         172.0(4)         -6.2         173.5(4)         -1.60           Ow1-H1a-O3'         171.8(6)         172.5(4)         -0.7         173.1(4)         -0.60           Ow2-H2a-O4         125.7(6)         148.5(4)         -22.8         149.2(3)         -0.70           Ow2-H2b-O2         122.6(6)         129.0(4)         -6.4         131.5(3)         -2.50           Ow2-H2b-O2'         129.6(6)         133.6(4)         -4.0         131.0(3)         2.60           Ow3-H3a-O4         132.3(6)         143.6(3)         -11.3         143.4(3)         0.20           Ow3-H3b-O1         173.7(5)         175.4(4)         -1.7         176.0(3)         -0.60 </td <td>O3-Ow1-O3'</td> <td>104.8(4)</td> <td>104.90 (11)</td> <td>-0.10</td> <td>104.46(10)</td> <td>0.44</td>	O3-Ow1-O3'	104.8(4)	104.90 (11)	-0.10	104.46(10)	0.44
O4-Ow3-O1         137.2(4)         136.23(13)         0.97         135.54(11)         0.69           Ow4-Ow3-O1         70.8(3)         70.28(10)         0.52         69.45(8)         0.83           O4-Ow4-O3         117.3(4)         116.68(12)         0.62         118.30(11)         -1.62           MSiD         0.43         0.055         0.805           MUD         0.63         0.805           Ow1-H1a-O3         165.8(5)         172.0(4)         -6.2         173.5(4)         -1.60           Ow1-H1b-O3'         171.8(6)         172.5(4)         -0.7         173.1(4)         -0.60           Ow2-H2a-O4         125.7(6)         148.5(4)         -22.8         149.2(3)         -0.70           Ow2-H2b-O2         122.6(6)         129.0(4)         -6.4         131.5(3)         -2.50           Ow2-H2b-O2'         129.6(6)         133.6(4)         -4.0         131.0(3)         2.60           Ow3-H3a-O4         132.3(6)         143.6(3)         -11.3         143.4(3)         0.20           Ow3-H3b-O1         173.7(5)         175.4(4)         -1.7         176.0(3)         -0.60           Ow4-H4a-O4         149.2(6)         156.7(4)         -7.5         156.4(3)	O4-Ow2-O2	144.5(4)	143.43(14)	1.07	142.81(12)	0.62
Ow4-Ow3-O1         70.8(3)         70.28(10)         0.52         69.45(8)         0.83           O4-Ow4-O3         117.3(4)         116.68(12)         0.62         118.30(11)         -1.62           MSiD         0.43         0.055           MUD         0.63         0.805           Ow1-H1a-O3         165.8(5)         172.0(4)         -6.2         173.5(4)         -1.60           Ow1-H1b-O3'         171.8(6)         172.5(4)         -0.7         173.1(4)         -0.60           Ow2-H2a-O4         125.7(6)         148.5(4)         -22.8         149.2(3)         -0.70           Ow2-H2b-O2         122.6(6)         129.0(4)         -6.4         131.5(3)         -2.50           Ow2-H2b-O2'         129.6(6)         133.6(4)         -4.0         131.0(3)         2.60           Ow3-H3a-O4         132.3(6)         143.6(3)         -11.3         143.4(3)         0.20           Ow3-H3b-O1         173.7(5)         175.4(4)         -1.7         176.0(3)         -0.60           Ow4-H4a-O4         149.2(6)         156.7(4)         -7.5         156.4(3)         0.30           Ow4-H4b-O3         141.8(5)         172.6(4)         -30.8         172.2(3)         0.40	O4-Ow2-O2'	92.6(3)		-0.52	93.75(9)	-0.63
O4-Ow4-O3 MSiD         117.3(4)         116.68(12)         0.62 0.43         118.30(11)         -1.62 0.055           MUD         0.63         0.805           Ow1-H1a-O3         165.8(5)         172.0(4)         -6.2         173.5(4)         -1.60           Ow2-H2a-O4         125.7(6)         172.5(4)         -0.7         173.1(4)         -0.60           Ow2-H2b-O2         122.6(6)         129.0(4)         -6.4         131.5(3)         -2.50           Ow3-H3a-O4         132.3(6)         143.6(3)         -11.3         143.4(3)         0.20           Ow3-H3a-Ow4         127.7(6)         124.0(3)         3.7         123.6(3)         0.40           Ow3-H3a-O4         149.2(6)         156.7(4)         -1.7         176.0(3)         -0.60           Ow4-H4a-O4         149.2(6)         156.7(4)         -7.5         156.4(3)         0.30           Ow4-H4b-O3         141.8(5)         172.6(4)         -30.8         172.2(3)         0.40           MSID         -8.77         -0.20           MUD         9.51         0.980	O4-Ow3-O1	137.2(4)	136.23(13)	0.97	135.54(11)	0.69
MSiD MUD         0.43 0.63         0.055 0.805           Ow1-H1a-O3 0W1-H1b-O3'         165.8(5) 172.0(4)         -6.2 -6.2         173.5(4) 173.5(4)         -1.60 -0.60           Ow2-H2a-O4 0w2-H2a-O4         125.7(6) 125.7(6)         148.5(4) 129.0(4)         -6.4 131.5(3)         149.2(3) -0.70         -0.70           Ow2-H2b-O2         122.6(6) 129.0(4)         -6.4 131.5(3)         131.5(3) 2.60         -2.50           Ow3-H3a-O4         132.3(6) 127.7(6)         143.6(3) 124.0(3)         -11.3 3.7         143.4(3) 123.6(3)         0.20           Ow3-H3b-O1 0w3-H3b-O1         173.7(5) 173.7(5)         175.4(4) 175.4(4)         -1.7 176.0(3)         -0.60 176.4(3)         0.30 0w4-H4a-O4         149.2(6) 149.2(6)         156.7(4) 172.6(4)         -30.8 172.2(3)         172.2(3) 0.40         0.40 0w4-H4b-O3         141.8(5) 172.6(4)         -8.77 9.51         -0.20 0.980		70.8(3)	70.28(10)	0.52	69.45(8)	0.83
MUD         0.63         0.805           Ow1-H1a-O3         165.8(5)         172.0(4)         -6.2         173.5(4)         -1.60           Ow1-H1b-O3'         171.8(6)         172.5(4)         -0.7         173.1(4)         -0.60           Ow2-H2a-O4         125.7(6)         148.5(4)         -22.8         149.2(3)         -0.70           Ow2-H2b-O2         122.6(6)         129.0(4)         -6.4         131.5(3)         -2.50           Ow2-H2b-O2'         129.6(6)         133.6(4)         -4.0         131.0(3)         2.60           Ow3-H3a-O4         132.3(6)         143.6(3)         -11.3         143.4(3)         0.20           Ow3-H3b-O1         173.7(5)         175.4(4)         -1.7         176.0(3)         -0.60           Ow4-H4a-O4         149.2(6)         156.7(4)         -7.5         156.4(3)         0.30           Ow4-H4b-O3         141.8(5)         172.6(4)         -30.8         172.2(3)         0.40           MSID         -8.77         -0.20           MUD         9.51         0.980	O4-Ow4-O3	117.3(4)	116.68(12)	0.62	118.30(11)	-1.62
Ow1-H1a-O3         165.8(5)         172.0(4)         -6.2         173.5(4)         -1.60           Ow1-H1b-O3'         171.8(6)         172.5(4)         -0.7         173.1(4)         -0.60           Ow2-H2a-O4         125.7(6)         148.5(4)         -22.8         149.2(3)         -0.70           Ow2-H2b-O2         122.6(6)         129.0(4)         -6.4         131.5(3)         -2.50           Ow2-H2b-O2'         129.6(6)         133.6(4)         -4.0         131.0(3)         2.60           Ow3-H3a-O4         132.3(6)         143.6(3)         -11.3         143.4(3)         0.20           Ow3-H3a-Ow4         127.7(6)         124.0(3)         3.7         123.6(3)         0.40           Ow3-H3b-O1         173.7(5)         175.4(4)         -1.7         176.0(3)         -0.60           Ow4-H4a-O4         149.2(6)         156.7(4)         -7.5         156.4(3)         0.30           Ow4-H4b-O3         141.8(5)         172.6(4)         -30.8         172.2(3)         0.40           MSiD         -8.77         -0.20           MUD         9.51         0.980	MSiD			0.43		0.055
Ow1-H1b-O3'         171.8(6)         172.5(4)         -0.7         173.1(4)         -0.60           Ow2-H2a-O4         125.7(6)         148.5(4)         -22.8         149.2(3)         -0.70           Ow2-H2b-O2         122.6(6)         129.0(4)         -6.4         131.5(3)         -2.50           Ow2-H2b-O2'         129.6(6)         133.6(4)         -4.0         131.0(3)         2.60           Ow3-H3a-O4         132.3(6)         143.6(3)         -11.3         143.4(3)         0.20           Ow3-H3a-Ow4         127.7(6)         124.0(3)         3.7         123.6(3)         0.40           Ow3-H3b-O1         173.7(5)         175.4(4)         -1.7         176.0(3)         -0.60           Ow4-H4a-O4         149.2(6)         156.7(4)         -7.5         156.4(3)         0.30           Ow4-H4b-O3         141.8(5)         172.6(4)         -30.8         172.2(3)         0.40           MSID         -8.77         -0.20           MUD         9.51         0.980	MUD			0.63		0.805
Ow2-H2a-O4         125.7(6)         148.5(4)         -22.8         149.2(3)         -0.70           Ow2-H2b-O2         122.6(6)         129.0(4)         -6.4         131.5(3)         -2.50           Ow2-H2b-O2'         129.6(6)         133.6(4)         -4.0         131.0(3)         2.60           Ow3-H3a-O4         132.3(6)         143.6(3)         -11.3         143.4(3)         0.20           Ow3-H3a-Ow4         127.7(6)         124.0(3)         3.7         123.6(3)         0.40           Ow3-H3b-O1         173.7(5)         175.4(4)         -1.7         176.0(3)         -0.60           Ow4-H4a-O4         149.2(6)         156.7(4)         -7.5         156.4(3)         0.30           Ow4-H4b-O3         141.8(5)         172.6(4)         -30.8         172.2(3)         0.40           MSID         -8.77         -0.20           MUD         9.51         0.980	Ow1-H1a-O3	165.8(5)	172.0(4)	-6.2	173.5(4)	-1.60
Ow2-H2b-O2         122.6(6)         129.0(4)         -6.4         131.5(3)         -2.50           Ow2-H2b-O2'         129.6(6)         133.6(4)         -4.0         131.0(3)         2.60           Ow3-H3a-O4         132.3(6)         143.6(3)         -11.3         143.4(3)         0.20           Ow3-H3a-Ow4         127.7(6)         124.0(3)         3.7         123.6(3)         0.40           Ow3-H3b-O1         173.7(5)         175.4(4)         -1.7         176.0(3)         -0.60           Ow4-H4a-O4         149.2(6)         156.7(4)         -7.5         156.4(3)         0.30           Ow4-H4b-O3         141.8(5)         172.6(4)         -30.8         172.2(3)         0.40           MSiD         -8.77         -0.20           MUD         9.51         0.980	Ow1-H1b-O3'	171.8(6)	172.5(4)	-0.7	173.1(4)	-0.60
Ow2-H2b-O2'         129.6(6)         133.6(4)         -4.0         131.0(3)         2.60           Ow3-H3a-O4         132.3(6)         143.6(3)         -11.3         143.4(3)         0.20           Ow3-H3a-Ow4         127.7(6)         124.0(3)         3.7         123.6(3)         0.40           Ow3-H3b-O1         173.7(5)         175.4(4)         -1.7         176.0(3)         -0.60           Ow4-H4a-O4         149.2(6)         156.7(4)         -7.5         156.4(3)         0.30           Ow4-H4b-O3         141.8(5)         172.6(4)         -30.8         172.2(3)         0.40           MSiD         -8.77         -0.20           MUD         9.51         0.980	Ow2-H2a-O4	125.7(6)	148.5(4)	-22.8	149.2(3)	-0.70
Ow3-H3a-O4         132.3(6)         143.6(3)         -11.3         143.4(3)         0.20           Ow3-H3a-Ow4         127.7(6)         124.0(3)         3.7         123.6(3)         0.40           Ow3-H3b-O1         173.7(5)         175.4(4)         -1.7         176.0(3)         -0.60           Ow4-H4a-O4         149.2(6)         156.7(4)         -7.5         156.4(3)         0.30           Ow4-H4b-O3         141.8(5)         172.6(4)         -30.8         172.2(3)         0.40           MSiD         -8.77         -0.20           MUD         9.51         0.980	Ow2-H2b-O2	122.6(6)	129.0(4)	-6.4		-2.50
Ow3-H3a-Ow4         127.7(6)         124.0(3)         3.7         123.6(3)         0.40           Ow3-H3b-O1         173.7(5)         175.4(4)         -1.7         176.0(3)         -0.60           Ow4-H4a-O4         149.2(6)         156.7(4)         -7.5         156.4(3)         0.30           Ow4-H4b-O3         141.8(5)         172.6(4)         -30.8         172.2(3)         0.40           MSID         -8.77         -0.20           MUD         9.51         0.980	Ow2-H2b-O2'	129.6(6)	133.6(4)	-4.0	131.0(3)	2.60
Ow3-H3b-O1     173.7(s)     175.4(4)     -1.7     176.0(3)     -0.60       Ow4-H4a-O4     149.2(6)     156.7(4)     -7.5     156.4(3)     0.30       Ow4-H4b-O3     141.8(s)     172.6(4)     -30.8     172.2(3)     0.40       MSiD     -8.77     -0.20       MUD     9.51     0.980			(- ,	-11.3	(- ,	0.20
Ow4-H4a-O4     149.2(6)     156.7(4)     -7.5     156.4(3)     0.30       Ow4-H4b-O3     141.8(5)     172.6(4)     -30.8     172.2(3)     0.40       MSiD     -8.77     -0.20       MUD     9.51     0.980						
Ow4-H4b-O3     141.8(5)     172.6(4)     -30.8     172.2(3)     0.40       MSiD     -8.77     -0.20       MUD     9.51     0.980		173.7(5)	175.4(4)		176.0(3)	-0.60
MSiD -8.77 -0.20 MUD 9.51 0.980		, ,	. ,	-7.5	156.4(3)	
MUD 9.51 0.980		141.8(5)	172.6(4)		172.2(3)	
<sup>a</sup> Refers to the difference between Baur (1962) and this study's 290 K structure.	MUD			9.51		0.980
	<sup>a</sup> Refers to the d	ifference betw	een Baur (196	2) and this	study's 290 K	structure.

before to the difference between Baur (1962) and this study's 290 K structure.

Befors to the difference of this study's 290 and 21 K structures, thus elucidating the influence of temperature on the respective quantity.

<sup>&</sup>lt;sup>c</sup>The mean signed difference is defined as

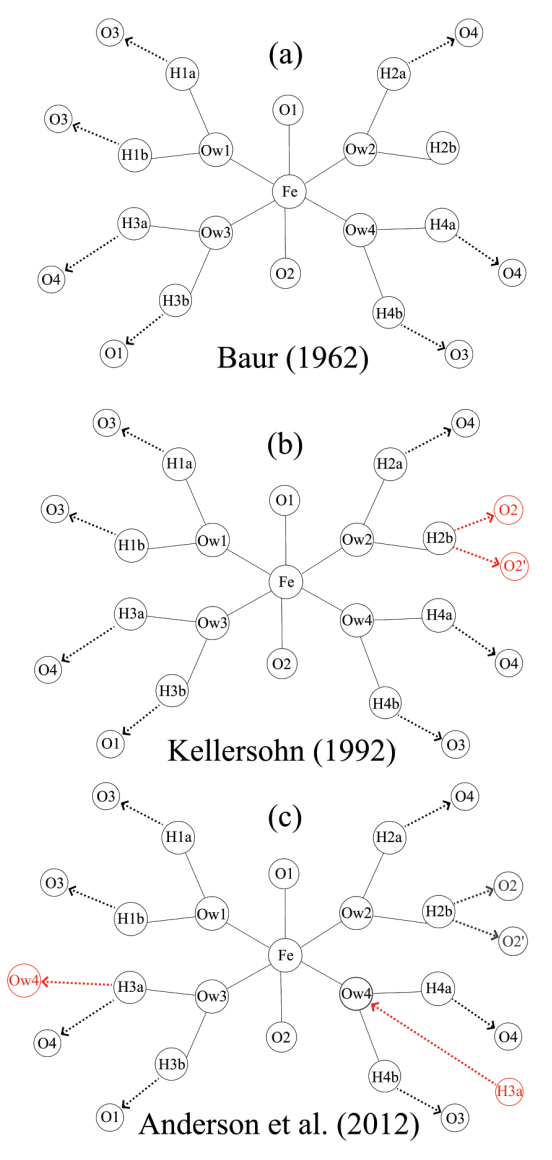


FIGURE 3. Interpretation of the hydrogen bond network by (a) Baur (1962) (b) Kellersohn (1992), and (c) Anderson et al. (2012). The changes suggested by these authors with respect to the previous interpretation are marked in red. (Color online.)

centered hydrogen bond in rozenite-type compounds, Anderson et al. (2012) suggested, based on an exhaustive comparison with numerous hydrogen bonding systems, that not only the H2b, but also the H3a atom is involved in a three-centered hydrogen bond (Ow3-H3a:::O4/Ow4) (Fig. 3c). According to our bond valance calculations the H3a···Ow4 contact exhibits a valency of 0.017, making it a weak but non-negligible hydrogen bond. Furthermore, when assessing the geometry of Ow3-H3a···Ow4 contact [i.e., H3a···Ow4 = 2.425(5) Å;  $\angle$ (Ow3-H3a···Ow4) = 124.0(3)° at 290 K], it is evident that this bond falls well within even the conservatively defined limits of hydrogen bonding [i.e., H···O <3 Å;  $\angle$ (Ow-H···O) = 110–180°; (Steiner 2002)]. Therefore, based on the large range of evidence in favor of three-centered hydrogen bonding involving the H3a and H2b atoms, we have adopted the

hydrogen bonding system proposed by Anderson et al. (2012) (Fig. 3c) for our study.

# Low-temperature crystallography, thermal expansion, and absence of phase transition

The powder diffraction data revealed no splitting of Bragg peaks nor appearance of new peaks that might be indicative of a phase transition. Consequently, the refined lattice parameters also varied smoothly (Fig. 4; Online Materials¹ Table S3 and S4). It is noteworthy that the  $\beta$  angle decreased systematically on cooling such that, at ~137 K, the unit-cell became metrically orthorhombic. However,  $\beta$  continued to decrease <90° below 137 K and it is important to emphasize that the Laue symmetry of the diffraction pattern retains its monoclinic character throughout the whole temperature range under investigation. Thus, rozenite does not undergo any structural phase transition down to at least 21 K.

There are various approaches to quantify the temperature dependency of the lattice parameters of crystalline solids, with varying degrees of usefulness and capability for accurate extrapolation. These range from polynomial fits through to parameterizations based on the classical Einstein model of the internal energy and the more accurate Debye-type model, which is used here.

The Debye model is derived from the Grüneisen relation of the thermoelastic properties:

$$\gamma = \alpha_V V K_0 / C_V \tag{1}$$

where  $\gamma$  is the Grüneisen ratio,  $\alpha_V$  is the volume thermal expansion coefficient,  $K_0$  is the isothermal bulk modulus,  $C_V$  is the isochoric specific heat capacity, and V the unit-cell volume. Equation 1 is integrated with respect to the temperature, whereby  $\gamma$  and  $K_0$  are assumed to be independent of the temperature. This yields the first-order approximation to the Grüneisen zero pressure equation of state which expresses the thermal expansion of the crystal as a function of its internal energy U(T) and isothermal bulk modulus  $K_0$ :

$$V(T) = V_0[1 + U(T)/Q]$$
 (2)

where  $Q = (V_0 K_0 / \gamma)$ .

U(T) may be derived by the Debye approximation:

$$U(T) = 9Nk_{\rm B}T \left(\frac{T}{\theta_{\rm D}}\right)^{3} \int_{0}^{\theta_{\rm D}/T} \frac{x^{3}}{e^{x} - 1} dx$$
 (3)

where N is the number of atoms per formula unit,  $k_B$  is Boltzmann constant,  $\theta_D$  is the Debye temperature, and  $x = \hbar \omega / k_B T$ . Note that the zero-point energy of  $9Nk_B\theta_D/8$  is included in Equation 2 via the term  $V_0$ .

It was apparent from the residuals obtained from fitting this model to V(T) that the first-order Grüneisen model failed to provide an accurate description of the thermal expansion (see Online Materials<sup>1</sup> Fig. S2). Consequently, we fitted a second-order approximation to the Grüneisen zero pressure equation of state (Eq. 4), which introduces the first derivative of the bulk modulus  $K'_0$  with respect to pressure via the parameter b:

$$V(T) = V_0 \{ 1 + U(T)/[Q - bU(T)] \}$$
(4)

where  $b = \frac{1}{2}(K'_0 - 1)$ .

The sum of squared residuals is thus reduced from  $0.32 \text{ Å}^6$  for the first-order fit to  $0.014 \text{ Å}^6$  for the second-order model.

The value of  $K_0/\gamma$  obtained from the second-order model is 84.5(4) GPa, increased from  $K_0 = 58.4(7)$  GPa in the poorer firstorder fit. We note that Meusburger et al. (2019) obtained a bulk modulus of 45.2(2) GPa for szomolnokite (FeSO<sub>4</sub>·H<sub>2</sub>O). It is highly unlikely that rozenite, featuring isolated cyclic [Fe(H<sub>2</sub>O)<sub>4</sub>SO<sub>4</sub>]<sub>2</sub> units loosely interconnected by intermolecular hydrogen bonds, exceeds the stiffness of szomolnokite featuring a rigid threedimensional framework structure. Fortes et al. (2006) report a bulk modulus of 21.5(1) GPa for epsomite (MgSO<sub>4</sub>·7H<sub>2</sub>O), a mineral featuring isolated Mg(H<sub>2</sub>O)<sub>6</sub> and SO<sub>4</sub> units loosely interconnected by hydrogen bonds. We should expect, therefore that rozenite will exhibit a compressibility intermediate between these hydrates, implying  $\gamma = 1.9$ –4.0. We further note that an extremely large value for K' of 41.1 as obtained from the second-order Debye fit clearly is unphysical but typical of the case where the complexity of the underlying phonon spectrum is represented by a simple model characterized with a single Debye frequency cut-off. The parameters derived from the second order single Debye fits are given in Table 4 and from the first order single Debye model in the Online Materials<sup>1</sup> Table S2. To be dimensionally correct, the individual lattice parameters were fitted as  $a^3$ ,  $b^3$ , and  $c^3$ .

For a more detailed assessment of the thermal expansion of rozenite the orientation and magnitude of the principal axes (Fig. 5a) and components (Fig. 5b) of the thermal expansion tensor were calculated using the Win\_strain software (Angel 2011). Strain tensors were computed incrementally between consecutive data points using the finite Lagrangian strain definition. The reference temperatures correspond to the average of the temperatures of the two data points used to calculate the strains. The thermal expansion tensor is constrained to have the  $\alpha_2$  principal axis parallel to [010] and  $\alpha_1$  and  $\alpha_3$  lying in the (010) plane. The orientation of the crystallographic axes relative to the cartesian reference system as specified by the Institute of Radio Engineers (i.e.,  $X \parallel a^*$ ;  $Z \parallel c$ ) was used for all calculations.

Cross sections through the representation surface of the thermal expansion tensor, evaluated at 285 K (Fig. 6), allow us to understand the relationship to both the monoclinic lattice vectors and the underlying structural elements. The expansion parallel with the a and c directions of the crystal are similar. The thermal expansion ||b, however, is substantially larger (i.e.,  $\alpha_a$ :  $\alpha_b$ :  $\alpha_c = 1.00:2.19:1.60$ 

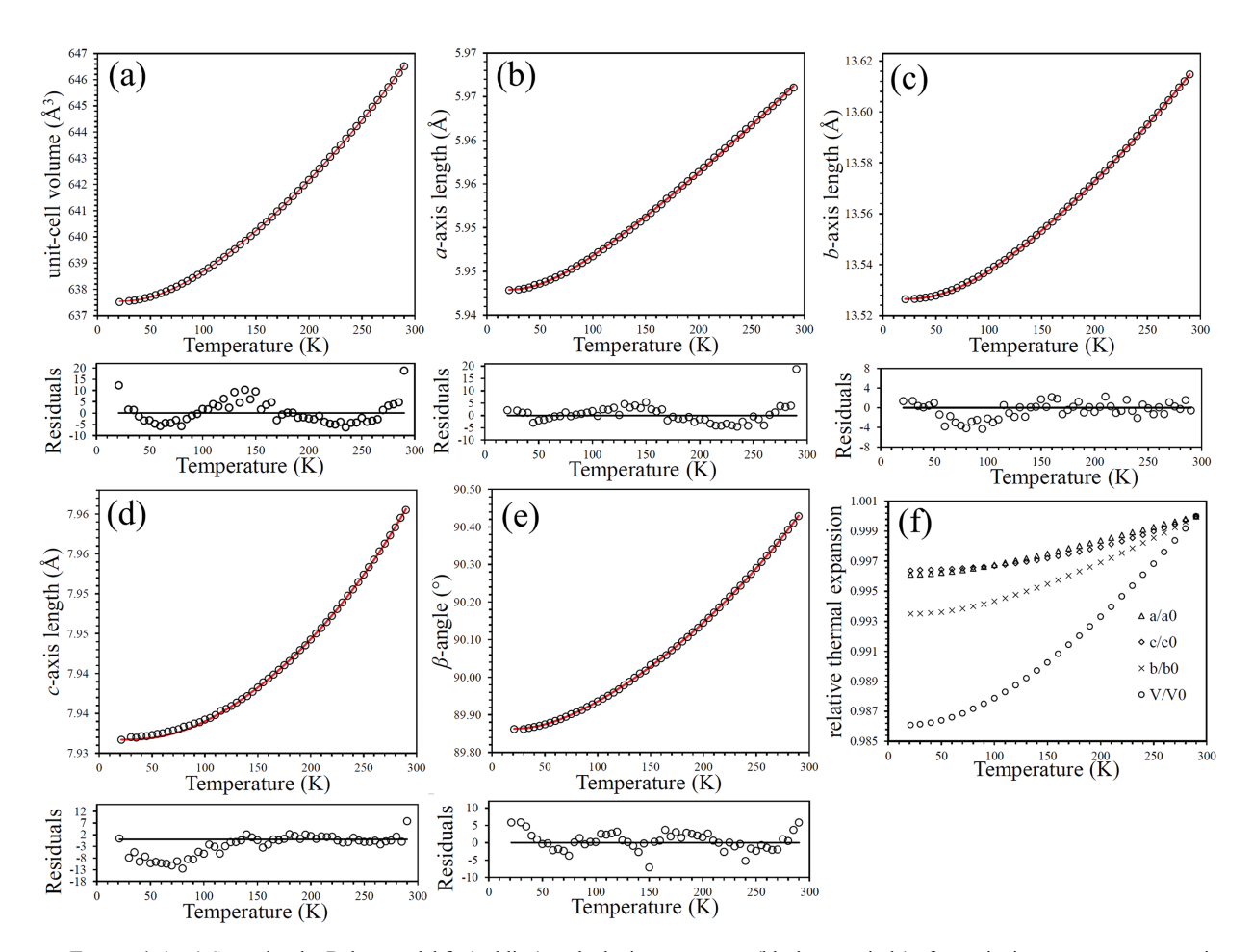


**FIGURE 4.** (a–e) Second-order Debye model fit (red line) to the lattice parameters (black open circle) of rozenite in at temperatures ranging from 290 to 21 K. Error bars are smaller than the symbol size. Residuals are defined as the difference between observed and fitted values divided by the experimental estimated standard deviation determined for each data point. (f) Relative thermal expansion of each of the lattice parameters as a function of temperature. Note the crossover in the evolution of the a and c axes ( $T \sim 100$  K). (Color online.)

**TABLE 4.** Parameters derived from fitting a second-order single Debye model upon the lattice parameters of rozenite

	a³	b <sup>3</sup>	<b>C</b> <sup>3</sup>	β	V
$\theta_D(K)$	240(6)	303(2)	382(4)	381(13)	278(2)
$X_0$ (cm <sup>3</sup> mol <sup>-1</sup> )	31.5994(6)	372.182(2)	75.1823(4)	13.5290(4)	95.9829(4)
$X_0$ (Å, Å <sup>3</sup> )	5.9428(1)	13.5214(8)	7.9337(5)	934(19)	637.533(3)
$Q (\times 10^4 \text{ J cm}^{-3})$	850(15)	519(3)	1047(12)	1263(26)	811.(3)
$K_0/\gamma$ (GPa)	269(5)	13.94(7)	139(2)	1617(17)	84.5(4)
K'	12.6	19.92	90.76	146.55	41.11

at 285 K). This behavior may be attributed to a large structural "void" and the absence of hydrogen bonding between the rigid cyclic dimer units  $\parallel b$  enabling the structure to undergo greater expansion in this direction upon heating (Fig. 6a).

Mapping of the thermal expansion onto the crystallographic reference frame conceals the true extent of the anisotropy, manifested in the eigenvalues and eigenvectors of the expansion tensor, i.e., the principal thermoelastic strains,  $\alpha_1:\alpha_2:\alpha_3=-1.00:3.74:5.40$ at 285 K. The principal axis  $\alpha_1$ , which is approximately oriented parallel to the (101) direction  $[a \angle 40.6(3)^{\circ} b \angle 90^{\circ} c \angle 49.8(3)^{\circ}]$ , exhibits negative thermal expansion over the entire temperature range under investigation. Contrary to this behavior,  $\alpha_3$ , oriented approximately  $\|\langle 10\overline{1}\rangle [a \angle 49.4(3)^{\circ} b \angle 90^{\circ} c \angle 139.8(3)^{\circ}]$  is the true direction of maximum thermal expansion. The stark contrast between the negative thermal expansion approximately | (101) and the direction of maximum expansion approximately  $\|\langle 10\overline{1}\rangle$ originates from the evolution of  $\beta$  with temperature. Shrinkage of  $\beta$ , the angle spanning the (100) and (001) directions, is mirrored by a simultaneous increase of the complementary angle spanning the  $\langle 100 \rangle$  and  $\langle 00\overline{1} \rangle$  directions (Fig. 6b). From a structural perspective an angle β close to 90° results in adjacent cyclic dimers being almost perfectly stacked on top of each other both in the a and c direction, despite this is not being a requirement imposed by symmetry. The evolution of  $\beta$  may then be explained as being due to a subtle displacement of the cyclic dimers relative to each other as a function of temperature (Fig. 6b.). Furthermore, the distances between the central atoms of the diagonally opposing FeO<sub>2</sub>(H<sub>2</sub>O)<sub>4</sub> and SO<sub>4</sub> units (Fig. 6b), are increasing upon cooling from 9.91385(3) Å (290 K) to 9.92414(3) Å (21 K) in the  $\langle 10\overline{1} \rangle$  direction (i.e., approximately  $\parallel \alpha_1$ ) and shrinking from 9.98531(3) Å (290 K) to 9.90118(3) Å (21 K) in the  $\langle 10\overline{1} \rangle$  (i.e., approximately  $\|\alpha_3$ ). Lastly, the relatively smaller thermal expansion in the *a* than the *c* direction (Fig. 6c) may be attributed to a denser population of the dimer units in this direction.

Comparing these findings to other hydrated sulfate minerals, it is evident that both large thermoelastic anisotropy and negative linear thermal expansion, in particular, is a common phenomenon in such materials. Negative linear expansion has been observed in epsomite (MgSO<sub>4</sub>·7H<sub>2</sub>O) (Fortes et al. 2006), meridianiite (MgSO<sub>4</sub>·11H<sub>2</sub>O) (Fortes et al. 2008), and most recently several members of the kieserite group ( $M^{2+}SO_4 \cdot H_2O$  with  $M^{2+} = Mg$ , Fe, Co, Ni) (Wildner et al. 2022). The negative thermal expansion found in our study is smaller than in MgSO<sub>4</sub>·7H<sub>2</sub>O, MgSO<sub>4</sub>·H<sub>2</sub>O, FeSO<sub>4</sub>·H<sub>2</sub>O, CoSO<sub>4</sub>·H<sub>2</sub>O and of approximately the same magnitude as in NiSO<sub>4</sub>·H<sub>2</sub>O and MgSO<sub>4</sub>·11H<sub>2</sub>O (Table 5). The volume thermal expansion of rozenite is intermediate between values found in the higher hydrates (e.g., MgSO<sub>4</sub>·7H<sub>2</sub>O and MgSO<sub>4</sub>·11H<sub>2</sub>O) and in the lower hydrates (e.g., FeSO<sub>4</sub>·H<sub>2</sub>O and MgSO<sub>4</sub>·H<sub>2</sub>O) (Table 5).

These trends in the volume thermal expansion reflect the changing degree of polymerization of the  $M^{2+}O_x(H_2O)_{6-x}$  and  $SO_4$  units as a function of hydration state, n, changing from isolated polyhedra (n = 6 to 11) through cyclic dimers and chains (n = 3 to 5) to rigid 3D corner-sharing frameworks (n = 1).

## Vibrational properties of rozenite and absence of phase transition

Hydrated sulfate minerals may de- or rehydrate under changing relative humidity conditions. Thus, it is possible that a sample or a fraction might transform after its identity and phase purity are confirmed by X-ray diffraction, and any subsequent measurements may not reflect the original state. Figures 7a and 7b displays a comparison of the Raman spectra as observed by Chio et al. (2007) and in this study, both inside and outside the glass capillary. Although the background is increased for the measurement performed through the borosilicate glass, a comparison with data collected outside of the capillary demonstrates that no additional sharp bands that might be mistaken for Raman-active vibrational modes appear in the spectrum (Fig. 7a).

Synchrotron X-ray diffraction analysis performed on the capil-

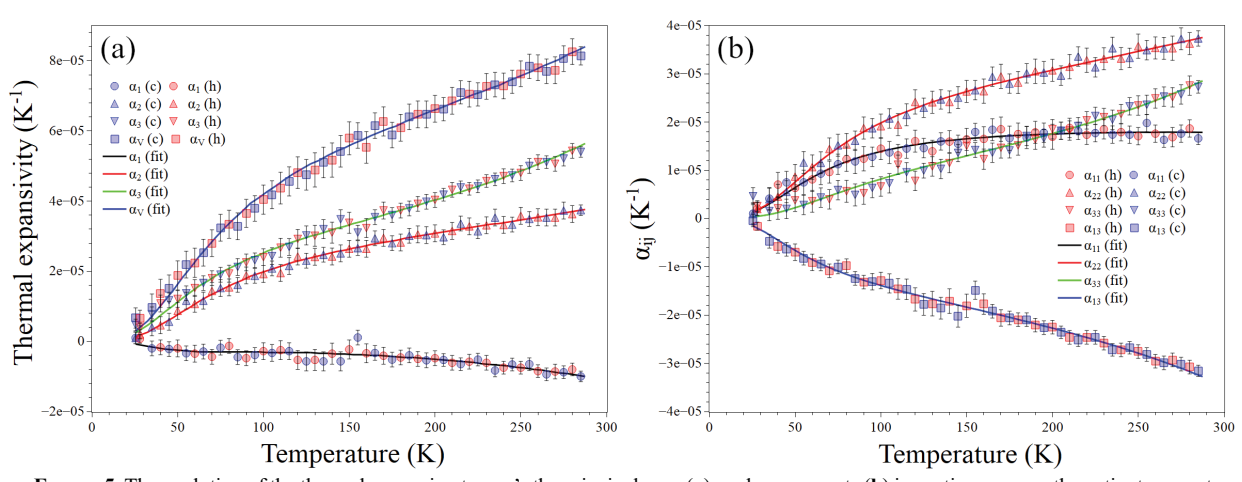


FIGURE 5. The evolution of the thermal expansion tensor's the principal axes (a), and components (b) is continuous over the entire temperature range under investigation. Solid lines represent the second-order Debye model fit; red and blue symbols are calculated from the lattice parameter data acquired upon heating and cooling respectively. Error bars were plotted as 3σ. (Color online.)

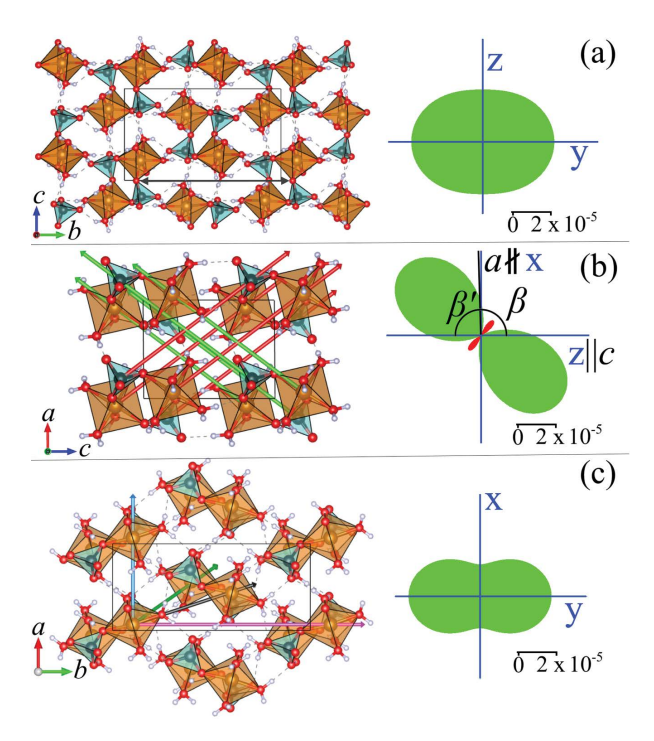


FIGURE 6. View of the crystal structure (left) and cross sections of the thermal expansion tensor (green represents positive, red negative values) at 285 K (right). (a) View  $\parallel$  a: Large "void" [black arrow: 11.932(5) Å at 290 K and 11.878(5) Å at 21 K]  $\parallel$  b as well as absence of hydrogen bonding in this direction allows the structure to experience substantial expansion and contraction in this direction as compared to the c-direction. (b) View  $\parallel$  b: red arrows point  $\parallel$  ⟨101⟩ (i.e., the direction of negative thermal expansion, whereas green arrows are oriented ⟨101⟩, i.e., the direction of maximum thermal expansion). The cyclic dimer units are stacked on top of each other and oriented by the angle of β (~90°). Furthermore, the distance between diagonally opposing Fe and S atoms (connected by the red and green arrows) is increasing upon cooling in the direction of negative thermal expansion and shrinking in the direction of maximum thermal expansion. (c) View  $\parallel$  c: arrows point toward to the central iron atoms of neighboring FeO<sub>2</sub>(H<sub>2</sub>O)<sub>4</sub> units. (Color online.)

lary sample confirms the phase purity of the material (Fig. 7c). As for the data collected by Chio et al. (2007), these authors noted that a shoulder at 1018 cm<sup>-1</sup> observed in their Raman spectra likely originate from szomolnokite impurities. A comparison of the Raman spectra collected in this study in and outside of the glass capillary shows the absence of the 1018 cm<sup>-1</sup> band for phase pure rozenite (Fig. 7b), thus confirming this hypothesis. For this reason, acquiring Raman spectra and performing X-ray diffraction on the same capillary, appears to be a suitable workflow to produce reliable fingerprint spectra for salt hydrate phases whose hydration state is susceptible to changes in relative humidity.

The neutron diffraction results clearly demonstrate the absence of any structural phase transition down to at least 21 K. This raises the question of how the vibrational mode splitting observed by Chio et al. (2007) may be explained. To understand this problem, we have computed the spatial frequencies of the Raman-active vibrational modes of rozenite from first principles (Fig. 8).

DFT predicts a total of 16 Raman-active vibrational modes in the region of the  $H_2O$  stretching modes (Fig. 8a). Therefore,

**TABLE 5.** Comparison of the negative (NTE) and volume (VTE) thermal expansion of various  $M^{2+}SO_4$ · $nH_2O$ 

	•					
Compound	NTE	$T_{ref}$	VTE expansion	$T_{ref}$	Source	
	(K <sup>-1</sup> )	(K)	(K <sup>-1</sup> )	(K)		
MgSO <sub>4</sub> ·11H₂O	$-1.2(5) \times 10^{-5}$	50	$6.8(4) \times 10^{-5}$	240	Fortes et al. (2008)	
MgSO <sub>4</sub> ·7H₂O	$-2.0(2) \times 10^{-5}$	125	$10.8(3) \times 10^{-5}$	290	Fortes et al. (2006)	
FeSO <sub>4</sub> ·4H₂O	$-1.0(2) \times 10^{-5}$	285	$8.2(5) \times 10^{-5}$	285	This study	
MgSO <sub>4</sub> ·H₂O	$-4.4(3) \times 10^{-5}$	293	$3.4(7) \times 10^{-5}$	293	Wildner et al. (2022)	
FeSO <sub>4</sub> ·H <sub>2</sub> O	$-1.7(2) \times 10^{-5}$	293	$4.7(5) \times 10^{-5}$	293	Wildner et al. (2022)	
CoSO <sub>4</sub> ·H <sub>2</sub> O	$-2.7(2) \times 10^{-5}$	293	$3.3(3) \times 10^{-5}$	293	Wildner et al. (2022)	
NiSO <sub>4</sub> ·H <sub>2</sub> O	$-0.8(5) \times 10^{-5}$	293	$3.6(4) \times 10^{-5}$	293	Wildner et al. (2022)	

assuming the occurrence of vibrational mode splitting and consequently a structural phase transition is not necessary to explain the 10 bands evidenced by Chio et al. (2007) at temperatures lower than 90 K. Furthermore, our computation suggests that several of the water stretching modes are overlapping; thus merely 10 instead of the total of 16 Raman-active modes are resolvable even at temperatures as low as 8 K.

The same holds true for the putative splitting of a mode located in the spectral region of the external vibrations (Fig. 8b), where our ab initio calculations also predict two Raman-active vibrational modes as closely spaced as 2.9 cm<sup>-1</sup>. Therefore, we conclude that the putative splitting of vibrational modes is a misinterpretation of the sharpening of these modes upon cooling.

Both our DFT calculations and group theoretical analysis within the  $C_{2h}$  point group using the SAM tool (Kroumova et al. 2003) as implemented in the Bilbao Crystallographic Server (Aroyo et al. 2006) predict a total of 108 Raman active modes (54A<sub>g</sub> + 54B<sub>g</sub>). Since first principle calculations at the  $\Gamma$ -point also yield the frequency of the IR-active modes as well as of the acoustic phonon modes, we further note that rozenite exhibits 105 IR active optical modes (53A<sub>n</sub> + 52B<sub>n</sub>) as well as 3 (A<sub>u</sub> + 2B<sub>u</sub>) acoustic phonon modes, totaling to 216 phonon modes of which 213 may be assigned to the optical branch and 3 to the acoustic one. The frequency and symmetry for each of the Raman (Online Materials<sup>1</sup> Table S5) and IR-active (Online Materials<sup>1</sup> Table S6) vibrational modes computed from first principles are provided in the Online Materials<sup>1</sup>. Ruggiero et al. (2015) have also modeled the vibrational properties of rozenite from first principles and curiously reported a total of 213 IRactive vibrational modes [Table S3 in supplementary material of Ruggiero et al. (2015)], at odd with both our first principles calculations as well as our group theoretical analysis. Based on the very low intensity reported for several modes i.e., of the 32 modes in the O-H stretching region 16 exhibit an intensity of <5% of the strongest IR active O-H stretching mode, and a total number of 213 IR-active modes which corresponds to the number of optical modes obtained in our study, we believe that Ruggiero et al. (2015) computed the  $\Gamma$ -point frequencies of the complete set of optical vibrational modes but wrongly assigned them all to be IR-active. Comparing the vibrational frequencies of the O-H stretching modes obtained by Ruggiero et al. (2015) (i.e., 3451.2–3807.3 cm<sup>-1</sup>) and the ones computed in our study (3278.7-3635.3 cm<sup>-1</sup>) to the experimental values (3252-3582 cm<sup>-1</sup>), it is evident that our calculations predict the vibrational mode frequencies much more accurately. Ruggiero et al. (2015) computed the vibrational frequencies at a higher level of theory and substantially higher computational cost using the B3LYP hybrid functional, yet again proving the effectiveness of the self-consistent DFT+U approach (Kulik et al. 2006; Timrov et al.

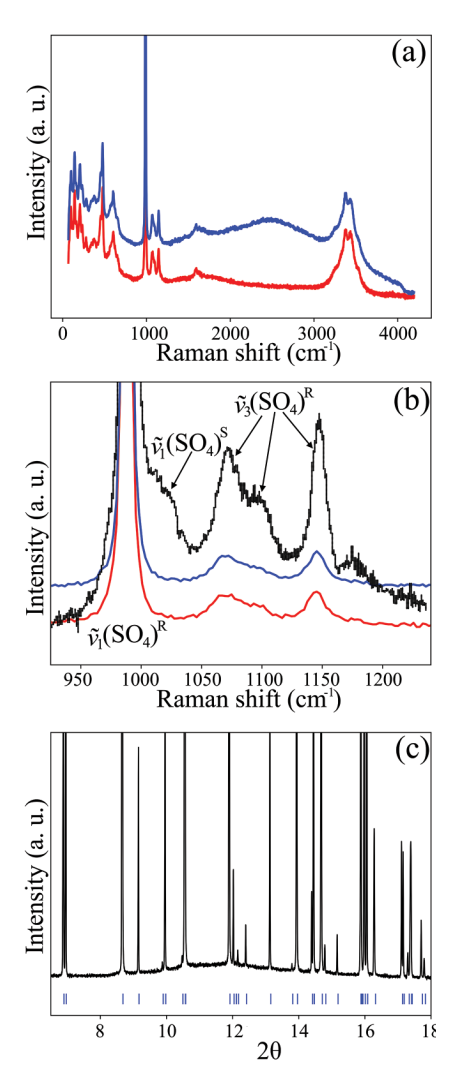


**FIGURE 7.** (a) Raman spectra acquired in this study outside (red) and inside (blue) of a borosilicate glass capillary. (b) Selected spectral range for comparison between our data (red and blue curves) and Chio et al. (2007) (black curve). (c) The phase purity of our sample has been confirmed by means of synchrotron X-ray diffraction, suggesting that the shoulder at 1018 cm<sup>-1</sup> in the Chio et al. (2007) spectrum (black) stems from a contamination of the sample with szomolnokite.  $\tilde{\nu}(SO_4)^R$  and  $\tilde{\nu}(SO_4)^S$  refer to the sulfate stretching modes assigned to rozenite and szomolnokite, respectively. The Raman spectrum reported by Chio et al. (2007) was digitized using the WebPlotDigitizer tool (Rohatgi 2021). The intensity in all graphs was normalized with respect to the maximum intensity. (Color online.)

2021) in accurately predicting the material properties of transition metal compounds at a fraction of the computational cost.

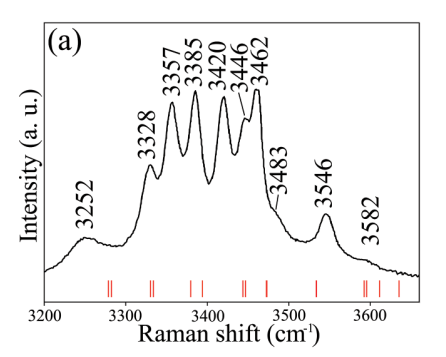
### **IMPLICATIONS**

We have demonstrated, by combining neutron diffraction with ab initio calculation within the framework of DFT, that the known monoclinic phase of rozenite is structurally stable over the entire temperature range it might be exposed to on the Martian surface and does not undergo any structural phase transition down to temperatures of at least 21 K. Rozenite is among the most

promising candidates for the polyhydrated sulfate phase on the Martian surface. Constraining the low-temperature stability and vibrational fingerprint of candidate phases such as rozenite is of vital importance to understand both the climatological history as well as for the future colonization of Mars. Characterization of the stratigraphic sequence (i.e., sulfate vs. clay mineral layers) of the polyhydrated sulfate deposits may enable us to decipher the nature, drivers, and onset of changing environmental conditions during the planet's early history.

As for the future colonization of Mars, hydrated sulfate minerals may be a valuable resource in the equatorial region where water ice is unstable (Feldman et al. 2004). Therefore, it is not only important to merely delineate between various mineral families, but a detailed mineralogical phase identification, including the mineral's hydration state, is crucial. For instance, 321 mL of water may be extracted from one kg rozenite, whereas complete dehydration of the same amount of the monohydrate yields 106 mL. Moreover, rozenite may be dehydrated to szomolnokite at 315 K, producing 241 mL H<sub>2</sub>O/kg, whereas complete desiccation of szomolnokite to anhydrous FeSO<sub>4</sub> takes place at a much higher temperature (~500 K) (Kanari et al. 2018). In contrast, the dehydration of rozenite to szomolnokite is a more efficient process, thus making it a potentially valuable resource for the extraction of water on Mars.

Raman spectroscopy has proven to be a very effective tool in discriminating between the various hydrated mineral species (Košek et al. 2017), but such efficacy relies on an accurate spectral library of the most promising candidate phases. As part of the



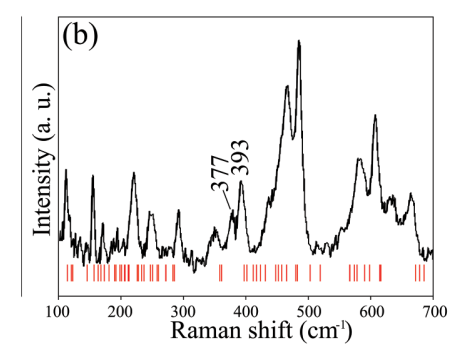


FIGURE 8. Spectral region of the (a) water stretching vibration and (b) external modes of the Raman spectrum acquired by Chio et al. (2007) at 8 K. Red markers indicate the Raman-active vibrational mode positions as predicted by DFT. The Raman spectrum reported by Chio et al. (2007) was digitized using the Webplotdigitizer tool (Rohatgi 2021). (Color online.)

scientific payload of the Perseverance rover, the first two Raman spectrometers were successfully deployed on the Martian surface (Bhartia et al. 2021; Wiens et al. 2021). The European Space Agency's Rosalind Franklin Rover (Rull et al. 2017), which is expected to land on the Martian surface in 2023, will also rely on Raman spectroscopy for mineralogical phase identification. Accurate vibrational fingerprint data are becoming increasingly important in planetary exploration. In our study, we have demonstrated that the challenges associated with the sensitivity of the sample material to changing relative humidity conditions may be circumvented by analyzing the sample inside a glass capillary and performing synchrotron X-ray diffraction on the very same capillary. Lastly, we want to highlight the role DFT may play in vibrational mode assignment and interpretation, in particular at low temperatures where the sharpening of vibrational modes might be misinterpreted as mode splitting. This will become even more important in the future as computational resources become cheaper and more readily available, and likewise, quantum mechanical modeling codes become increasingly user-friendly and optimized for high-throughput calculations. Combining such calculations with experimentally determined reference spectra will enable the construction of a reliable Raman spectroscopic database for planetary exploration, which will be invaluable to shed light on the geological past as well as in identifying resources for the future colonization of planetary bodies in the solar system.

#### ACKNOWLEDGMENTS AND FUNDING

We want to thank STFC's Scientific Computing Department for the provision of computing resources on the SCARF cluster and, in particular, Jon Roddom for compiling the Quantum ESPRESSO code. Moreover, we want to thank two anonymous reviewers for their thorough reading and constructive feedback. We further acknowledge the STFC for access to beamtime at the ISIS Neutron and Muon Source (RB2010354) and the Diamond Light Source (CY26409). J.M.M. acknowledges funding from an ISIS Facility Development and Utilisation Studentship (50%) and the University of Exeter (50%).

#### REFERENCES CITED

- Albinati, A. and Willis, B.T.M. (1982) The Rietveld method in neutron and X-ray powder diffraction. Journal of Applied Crystallography, 15, 361–374, https://doi.org/10.1107/S0021889882012187.
- Alig, H., Losel, J., and Trömel, M. (1994) Zur Kristallchemie der Wasserstoff–Sauerstoff-Bindungen. Zeitschrift für Kristallographie, 209, 18–21, https://doi.org/10.1524/zkri.1994.209.1.18.
- Amadon, B., Jollet, F., and Torrent, M. (2008) γ and β cerium: LDA+U calculations of ground-state parameters. Physical Review B, 77, 155104, https://doi.org/10.1103/PhysRevB.77.155104.
- Anderson, J.L., Peterson, R.C., and Swainson, I. (2012) The atomic structure of deuterated boyleite ZnSO<sub>4</sub>·4D<sub>2</sub>O, ilesite MnSO<sub>4</sub>·4D<sub>2</sub>O, and bianchite ZnSO<sub>4</sub>·6D<sub>2</sub>O. American Mineralogist, 97, 1905–1914, https://doi.org/10.2138/am.2012.4121.
- Angel, R.J. (2011) Win\_Strain4. Padova. http://www.rossangel.com/text\_strain.htm (Accessed April 20, 2023).
- Aroyo, M.I., Perez-Mato, J.M., Capillas, C., Kroumova, E., Ivantchev, S., Madariaga, G., Kirov, A., and Wondratschek, H. (2006) Bilbao Crystallographic Server: I. Databases and crystallographic computing programs. Zeitschrift für Kristallographie, 221, 15–27, https://doi.org/10.1524/zkri.2006.221.1.15.
- Baur, W.H. (1962) Zur Kristallchemie der Salzhydrate. Die Kristallstrukturen von MgSO<sub>4</sub>.4H<sub>2</sub>O (leonhardtit) und FeSO<sub>4</sub>.4H<sub>2</sub>O (rozenit). Acta Crystallographica, 15, 815–826, https://doi.org/10.1107/S0365110X62002200.
- ———(1964) On the crystal chemistry of salt hydrates. II. A neutron diffraction study of MgSO<sub>4</sub>.4H<sub>2</sub>O. Acta Crystallographica, 17, 863–869, https://doi.org/10.1107/S0365110X64002304.
- ——— (1972) Prediction of hydrogen bonds and hydrogen atom positions in crystalline solids. Acta Crystallographica B, 28, 1456–1465, https://doi.org/10.1107/ S0567740872004455.
- ——— (2002) Zinc(II) sulfate tetrahydrate and magnesium sulfate tetrahydrate Addendum. Acta Crystallographica. Section E, Structure Reports Online, 58, e9–e10, https://doi.org/10.1107/S1600536802002192.
- Bhartia, R., Beegle, L.W., DeFlores, L., Abbey, W., Razzell Hollis, J., Uckert, K., Monacelli, B., Edgett, K.S., Kennedy, M.R., Sylvia, M., and others. (2021) Per-

- severance's scanning habitable environments with Raman and luminescence for organics and chemicals (SHERLOC) investigation. Space Science Reviews, 217, 58, https://doi.org/10.1007/s11214-021-00812-z.
- Bibring, J.-P., Langevin, Y., Gendrin, A., Gondet, B., Poulet, F., Berthé, M., Soufflot, A., Arvidson, R., Mangold, N., Mustard, J., and others. (2005) Mars surface diversity as revealed by the OMEGA/Mars Express observations. Science, 307, 1576–1581, https://doi.org/10.1126/science.1108806.
- Bibring, J.-P., Langevin, Y., Mustard, J.F., Poulet, F., Arvidson, R., Gendrin, A., Gondet, B., Mangold, N., Pinet, P., Forget, F., and others. (2006) Global mineralogical and aqueous mars history derived from OMEGA/Mars Express data. Science, 312, 400–404, https://doi.org/10.1126/science.1122659.
- Bishop, J.L., Parente, M., Weitz, C.M., Noe Dobrea, E.Z., Roach, L.H., Murchie, S.L., McGuire, P.C., McKeown, N.K., Rossi, C.M., Brown, A.J., and others. (2009) Mineralogy of Juventae Chasma: Sulfates in the light-toned mounds, mafic minerals in the bedrock, and hydrated silica and hydroxylated ferric sulfate on the plateau. Journal of Geophysical Research Planets, 114, E00D09.
- Brese, N.E. and O'Keeffe, M. (1991) Bond-valence parameters for solids. Acta Crystallographica, B47, 192–197, https://doi.org/10.1107/S01087681900 11041.
- Brown, I.D. and Altermatt, D. (1985) Bond-valence parameters obtained from a systematic analysis of the Inorganic Crystal Structure Database. Acta Crystallographica, B41, 244–247, https://doi.org/10.1107/S0108768185002063.
- Carter, J., Poulet, F., Bibring, J.-P., Mangold, N., and Murchie, S. (2013) Hydrous minerals on Mars as seen by the CRISM and OMEGA imaging spectrometers: Updated global view. Journal of Geophysical Research. Planets, 118, 831–858, https://doi.org/10.1029/2012JE004145.
- Chio, C., Sharma, S., and Muenow, D. (2007) The hydrates and deuterates of ferrous sulfate (FeSO<sub>4</sub>): A Raman spectroscopic study. Journal of Raman Spectroscopy, 38, 87–99, https://doi.org/10.1002/jrs.1623.
- Cococcioni, M. and de Gironcoli, S. (2005) Linear response approach to the calculation of the effective interaction parameters in the LDA+U method. Physical Review B: Condensed Matter and Materials Physics, 71, 035105, https://doi.org/10.1103/ PhysRevB.71.035105.
- Dudarev, S.L., Botton, G.A., Savrasov, S.Y., Humphreys, C.J., and Sutton, A.P. (1998) Electron-energy-loss spectra and the structural stability of nickel oxide: An LSDA+U study. Physical Review B: Condensed Matter, 57, 1505–1509, https://doi.org/10.1103/PhysRevB.57.1505.
- Feldman, W., Mellon, M., Maurice, S., Prettyman, T., Carey, B., Vaniman, D., Bish, D., Claire, F., Chipera, S., and Kargel, J. (2004) Hydrated states of MgSO<sub>4</sub> at equatorial latitudes on Mars. Geophysical Research Letters, 31, L16702–L16704, https://doi.org/10.1029/2004GL020181.
- Floris, A., de Gironcoli, S., Gross, E.K.U., and Cococcioni, M. (2011) Vibrational properties of MnO and NiO from DFT+U-based density functional perturbation theory. Physical Review B: Condensed Matter and Materials Physics, 84, 161102, https://doi.org/10.1103/PhysRevB.84.161102.
- Floris, A., Timrov, I., Himmetoglu, B., Marzari, N., de Gironcoli, S., and Cococcioni, M. (2020) Hubbard-corrected density functional perturbation theory with ultrasoft pseudopotentials. Physical Review B, 101, 064305, https://doi.org/10.1103/ PhysRevB.101.064305.
- Fortes, A.D., Wood, I.G., Alfredsson, M., Vočadlo, L., and Knight, K.S. (2006) The thermoelastic properties of MgSO<sub>4</sub>·7D<sub>2</sub>O (epsomite) from powder neutron diffraction and ab initio calculation. European Journal of Mineralogy, 18, 449–462, https://doi.org/10.1127/0935-1221/2006/0018-0449.
- Fortes, A.D., Wood, I., and Knight, K. (2008) The crystal structure and thermal expansion tensor of MgSO<sub>4</sub>:11D<sub>2</sub>O(meridianiite) determined by neutron powder diffraction. Physics and Chemistry of Minerals, 35, 207–221, https://doi.org/10.1007/s00269-008-0214-x.
- Garrity, K.F., Bennett, J.W., Rabe, K.M., and Vanderbilt, D. (2014) Pseudopotentials for high-throughput DFT calculations. Computational Materials Science, 81, 446–452, https://doi.org/10.1016/j.commatsci.2013.08.053.
- Giannozzi, P., Baroni, S., Bonini, N., Calandra, M., Car, R., Cavazzoni, C., Ceresoli, D., Chiarotti, G.L., Cococcioni, M., Dabo, I., and others. (2009) QUANTUM ESPRESSO: A modular and open-source software project for quantum simulations of materials. Journal of Physics Condensed Matter, 21, 395502, https://doi.org/10.1088/0953-8984/21/39/395502.
- Giannozzi, P., Andreussi, O., Brumme, T., Bunau, O., Buongiorno Nardelli, M., Calandra, M., Car, R., Cavazzoni, C., Ceresoli, D., Cococcioni, M., and others. (2017) Advanced capabilities for materials modelling with Quantum ESPRESSO. Journal of Physics Condensed Matter, 29, 465901, https://doi.org/10.1088/1361-648X/aa8f79.
- Gómez-Elvira, J., Armiens, C., Carrasco, I., Genzer, M., Gómez, F., Haberle, R., Hamilton, V.E., Harri, A.-M., Kahanpää, H., Kemppinen, O., and others. (2014) Curiosity's rover environmental monitoring station: Overview of the first 100 sols. Journal of Geophysical Research. Planets, 119, 1680–1688, https://doi.org/ 10.1002/2013JE004576.
- Greenspan, L. (1977) Humidity fixed points of binary saturated aqueous solutions. Journal of Research of the National Bureau of Standards. Section A. Physics and Chemistry, 81A, 89–96, https://doi.org/10.6028/jres.081A.011.
- Grimme, S. (2006) Semiempirical GGA-type density functional constructed with a longrange dispersion correction. Journal of Computational Chemistry, 27, 1787–1799, https://doi.org/10.1002/jcc.20495.

- Held, P. and Bohaty, L. (2002) Manganese(II) sulfate tetrahydrate (ilesite). Acta Crystallographica, E58, i121–i123, https://doi.org/10.1107/S1600536802020962.
- Hohenberg, P. and Kohn, W. (1964) Inhomogeneous electron gas. Physical Review, 136 (3B), B864–B871, https://doi.org/10.1103/PhysRev.136.B864.
- Hudson-Edwards, K.A., Schell, C., and Macklin, M.G. (1999) Mineralogy and geochemistry of alluvium contaminated by metal mining in the Rio Tinto area, southwest Spain. Applied Geochemistry, 14, 1015–1030, https://doi.org/10.1016/ S0883-2927(99)00008-6.
- Jambor, J., Nordstrom, D., and Alpers, C. (2000) Metal-sulfate salts from sulfide mineral oxidation. Reviews in Mineralogy and Geochemistry, 40, 303–350, https://doi.org/ 10.2138/rmg.2000.40.6.
- Kanari, N., Menad, N.-E., Ostrosi, E., Shallari, S., Diot, F., Allain, E., and Yvon, J. (2018) Thermal behavior of hydrated iron sulfate in various atmospheres. Metals, 8, 1084, https://doi.org/10.3390/met8121084.
- Kellersohn, T. (1992) Structure of cobalt sulfate tetrahydrate. Acta Crystallographica, C48, 776–779, https://doi.org/10.1107/S0108270191012003.
- Klingelhöfer, G., Morris, R.V., Bernhardt, B., Schröder, C., Rodionov, D.S., de Souza, P.A., Yen, A., Gellert, R., Evlanov, E.N., Zubkov, B., and others (2004) Jarosite and hematite at Meridiani Planum from Opportunity's Mössbauer Spectrometer. Science, 306, 1740–1745.
- Kohn, W. and Sham, L.J. (1965) Self-consistent equations including exchange and correlation effects. Physical Review, 140 (4A), A1133–A1138, https://doi.org/10.1103/PhysRev.140.A1133.
- Košek, F., Culka, A., Drahota, P., and Jehlička, J. (2017) Applying portable Raman spectrometers for field discrimination of sulfates: Training for successful extraterrestrial detection. Journal of Raman Spectroscopy, 48, 1085–1093, https://doi.org/ 10.1002/jrs.5174.
- Kroumova, E., Aroyo, M.I., Perez-Mato, J.M., Kirov, A., Capillas, C., Ivantchev, S., and Wondratschek, H. (2003) Bilbao crystallographic server: useful databases and tools for phase-transition studies. Phase Transitions, 76, 155–170, https://doi.org/10.1080/0141159031000076110.
- Kulik, H.J., Cococcioni, M., Scherlis, D.A., and Marzari, N. (2006) Density functional theory in transition-metal chemistry: A self-consistent Hubbard U approach. Physical Review Letters, 97, 103001, https://doi.org/10.1103/PhysRevLett.97.103001.
- Langevin, Y., Poulet, F., Douté, S., Vincendon, M., Bibring, J.-P., Gondet, B., Forget, F., Montmessin, F., and Schmitt, B. (2006) The Vis/NIR OMEGA imaging spectrometer on-board Mars Express. 36th COSPAR Scientific Assembly, Beijing, China. Abstract 2422
- Meusburger, J.M., Ende, M., Talla, D., Wildner, M., and Miletich, R. (2019) Transformation mechanism of the pressure-induced C2/c-to-P

  Transition in ferrous sulfate monohydrate single crystals. Journal of Solid State Chemistry, 277, 240–252, https://doi.org/10.1016/j.jssc.2019.06.004.
- Meusburger, J.M., Hudson-Edwards, K.A., Tang, C.C., Crane, R.A., and Fortes, A.D. (2021) Elasticity of selected icy satellite candidate materials (CO<sub>2</sub>, C<sub>6</sub>H<sub>6</sub>, MgSO<sub>4</sub>·7H<sub>2</sub>O and CaSO<sub>4</sub>·2H<sub>2</sub>O) revisited by dispersion corrected density functional theory. Icarus, 368, 114611, https://doi.org/10.1016/j.icarus.2021.114611.
- Meusburger, J.M., Hudson-Edwards, K.A., Tang, C.T., Connolly, E.T., Crane, R.A., and Fortes, A.D. (2022) Low-temperature crystallography and vibrational properties of rozenite (FeSO<sub>4</sub>·4H<sub>2</sub>O), a candidate mineral component of the polyhydrated sulfate deposits on Mars. Materials Cloud Archive.
- Mitchell, A.G. (1984) The preparation and characterization of ferrous sulphate hydrates. The Journal of Pharmacy and Pharmacology, 36, 506–510, https://doi.org/10.1111/j.2042-7158.1984.tb04440.x.
- Momma, K. and Izumi, F. (2011) VESTA3 for three-dimensional visualization of crystal, volumetric and morphology data. Journal of Applied Crystallography, 44, 1272–1276, https://doi.org/10.1107/S0021889811038970.
- Monkhorst, H.J. and Pack, J.D. (1976) Special points for Brillouin-zone integrations. Physical Review. B, Solid State, 13, 5188–5192, https://doi.org/10.1103/PhysRevB.13.5188.
- Nordstrom, D. (2011) Mine waters: Acidic to circumneutral. Elements, 7, 393-398.
- Perdew, J.P., Burke, K., and Ernzerhof, M. (1996) Generalized Gradient Approximation made simple. Physical Review Letters, 77, 3865–3868, https://doi.org/10.1103/ PhysRevLett.77.3865.
- Pfrommer, B.G., Cote, M., Louie, S.G., and Cohen, M.L. (1997) Relaxation of crystals with the quasi-Newton method. Journal of Computational Physics, 131, 233–240, https://doi.org/10.1006/jcph.1996.5612.
- Raczkowski, D., Canning, A., and Wang, L.W. (2001) Thomas-Fermi charge mixing for obtaining self-consistency in density functional calculations. Physical Review B: Condensed Matter, 64, 121101, https://doi.org/10.1103/PhysRevB.64.121101.
- Roach, L.H., Mustard, J.F., Swayze, G., Milliken, R.E., Bishop, J.L., Murchie, S.L., and Lichtenberg, K. (2010) Hydrated mineral stratigraphy of Ius Chasma, Valles Marineris. Icarus, 206, 253–268, https://doi.org/10.1016/j.icarus.2009.09.003.
- Rohatgi, A. (2021) WebPlotDigitizer: version 4.5. https://automeris.io/WebPlotDigitizer/

- (Accessed April 20, 2023).
- Ruggiero, M.T., Bardon, T., Strlič, M., Taday, P.F., and Korter, T.M. (2015) The role of terahertz polariton absorption in the characterization of crystalline iron sulfate hydrates. Physical Chemistry Chemical Physics, 17, 9326–9334, https://doi.org/ 10.1039/C5CP01195G.
- Rull, F., Maurice, S., Hutchinson, I., Moral, A., Perez, C., Diaz, C., Colombo, M., Belenguer, T., Lopez-Reyes, G., Sansano, A., and others. (2017) The Raman Laser Spectrometer for the ExoMars Rover Mission to Mars. Astrobiology, 17, 627–654, https://doi.org/10.1089/ast.2016.1567.
- Squyres, S.W., Grotzinger, J.P., Arvidson, R.E., Bell, J.F. III, Calvin, W., Christensen, P.R., Clark, B.C., Crisp, J.A., Farrand, W.H., Herkenhoff, K.E., and others. (2004) In situ evidence for an ancient aqueous environment at Meridiani Planum, Mars. Science, 306, 1709–1714, https://doi.org/10.1126/science.1104559.
- Steiner, T. (2002) The hydrogen bond in the solid state. Angewandte Chemie International Edition, 41, 48–76, https://doi.org/10.1002/1521-3773(20020104)41:1<48:AID-ANIE48>3.0.CO;2-U.
- Talla, D. and Wildner, M. (2019) Investigation of the kieserite–szomolnokite solid-solution series (Mg,Fe)SO<sub>4</sub>·H<sub>2</sub>O, with relevance to Mars: Crystal chemistry, FTIR, and Raman spectroscopy under ambient and Martian temperature conditions. American Mineralogist, 104, 1732–1749, https://doi.org/10.2138/am-2019-6983.
- Thompson, S.P., Parker, J.E., Potter, J., Hill, T.P., Birt, A., Cobb, T.M., Yuan, F., and Tang, C.C. (2009) Beamline II1 at Diamond: A new instrument for high resolution powder diffraction. The Review of Scientific Instruments, 80, 075107, https://doi.org/10.1063/1.3167217.
- Timrov, I., Marzari, N., and Cococcioni, M. (2018) Hubbard parameters from density-functional perturbation theory. Physical Review B, 98, 085127, https://doi.org/10.1103/PhysRevB.98.085127.
- ——(2021) Self-consistent Hubbard parameters from density-functional perturbation theory in the ultrasoft and projector-augmented wave formulations. Physical Review B, 103, 045141, https://doi.org/10.1103/PhysRevB.103.045141.
- Toby, B.H. (2001) EXPGUI, a graphical user interface for GSAS. Journal of Applied Crystallography, 34, 210–213, https://doi.org/10.1107/S0021889801002242.
- Tosca, N.J., McLennan, S.M., Clark, B.C., Grotzinger, J.P., Hurowitz, J.A., Knoll, A.H., Schröder, C., and Squyres, S.W. (2005) Geochemical modeling of evaporation processes on Mars: Insight from the sedimentary record at Meridiani Planum. Earth and Planetary Science Letters, 240, 122–148, https://doi.org/10.1016/j.epsl.2005.09.042.
- van Laar, B. and Schenk, H. (2018) The development of powder profile refinement at the Reactor Centre Netherlands at Petten. Acta Crystallographica, A74, 88–92, https://doi.org/10.1107/S2053273317018435.
- Wang, A., Jolliff, B.L., Liu, Y., and Connor, K. (2016) Setting constraints on the nature and origin of the two major hydrous sulfates on Mars: Monohydrated and polyhydrated sulfates. Journal of Geophysical Research. Planets, 121, 678–694, https:// doi.org/10.1002/2015JE004889.
- Wiens, R.C., Maurice, S., Robinson, S.H., Nelson, A.E., Cais, P., Bernardi, P., Newell, R.T., Clegg, S., Sharma, S.K., Storms, S., and others. (2021) The SuperCam Instrument Suite on the NASA Mars 2020 Rover: Body Unit and Combined System Tests. Space Science Reviews, 217, 4, https://doi.org/10.1007/s11214-020-00777-5.
- Wildner, M., Zakharov, B.A., Bogdanov, N.E., Talla, D., Boldyreva, E.V., and Miletich, R. (2022) Crystallography relevant to Mars and Galilean icy moons: Crystal behavior of kieserite-type monohydrate sulfates at extraterrestrial conditions down to 15 K. IUCrJ, 9, 194–203, https://doi.org/10.1107/S2052252521012720.

Manuscript received February 23, 2022 Manuscript accepted July 22, 2022 Accepted Manuscript online July 28, 2022 Manuscript Handled by Antonio M. dos Santos

#### **Endnote:**

<sup>1</sup>Deposit item AM-23-68502, Online Materials. Deposit items are free to all readers and found on the MSA website, via the specific issue's Table of Contents (go to http://www.minsocam.org/MSA/AmMin/TOC/2023/Jun2023\_data/Jun2023\_data.html). The CIF has been peer-reviewed by our Technical Editors.

<sup>2</sup>The MUD is defined as

$$\frac{\sum_{i}^{n} x_{\rm B} - x_{\rm T}}{}$$

. .

with  $x_B$  and  $x_T$  being the values as observed by Baur and in this study, respectively, for the quantities of interest (i.e., bond-length and angle).